SAND77-0944
NUREG-0183-2
Unlimited Release

Distribution
Category NRC-3

LIGHT WATER REACTOR SAFETY RESEARCH PROGRAM QUARTERLY REPORT OCTOBER - DECEMBER 1976

Nuclear Fuel Cycle Safety Research Department

Prepared by Sandia Laboratories, Albuquerque,
New Mexico 87115 and Livermore, California 94500
for the United States Nuclear Regulatory Commission
under ERDA Contract AT(29-1)-789.

Printed July 1977

Sandia Laboratories

Nuclear Fuel Cycle Programs

SF 190C (07-73)

Issued by Sandia Laboratories, operated for the United States Energy Research & Development Administration by Sandia Corporation.

Printed in the United States of America
Available from
National Technical Information Service
U. S. Department of Commerce
5285 Port Royal Road
Springfield, VA 22161
Price: Printed Copy $5.00; Microfiche $3.00

SAND77-0944
NUREG-0183-2
Unlimited Release
Printed July 1977

Distribution
Category NRC-3

LIGHT WATER REACTOR SAFETY RESEARCH PROGRAM*
QUARTERLY REPORT

October - December 1976

Submitted by

Nuclear Fuel Cycle Safety Research Department
Sandia Laboratories, Albuquerque, New Mexico 87115

Person in Charge: D. A. Dahlgren, 5411

APPROVED: D. J. McCloskey
Manager, Nuclear Fuel Cycle Safety Research

Director, Nuclear Fuel Cycle Programs

*This work is supported by the U. S. Nuclear Regulatory Commission (Project Nos. A-1019 and A-1030).

164 221

CONTENTS

764 222

ILLUSTRATIONS

ILLUSTRATIONS

764 224

TABLES

LIGHT WATER REACTOR SAFETY RESEARCH PROGRAM

1. Molten Core - Concrete Interactions Study

1.1 Summary

The Molten Core - Concrete Interactions Study was initiated in July 15, 1975, to provide a qualitative, scoping exploration of the phenomena associated with contact between molten core materials and concrete. The experimental elements of this study are divided into four categories:

1.1 Deposition of corium-type melts onto concrete.
1.2 Kinetics and stoichiometry of the thermal decomposition of concrete.
1.3 Response of concrete to high heat fluxes at one surface.
1.4 Simulation experiments which explore phenomena at the interface between a melt and a decomposing solid.

The experimental results are being incorporated in a scaling analysis which will establish scaling parameters for the system and identify key elements of the melt-concrete interaction. A complete project description of the study was issued in October 1975.

During this period one small-scale thermite test was performed. In addition, a preliminary model of the melt-concrete interaction process has been developed. The following paragraphs summarize the results for this quarter.

Small-Scale Melt-Concrete Interaction Test

One small-scale steel-concrete interaction test was conducted. The test was a successful demonstration of our test concept and test chamber. The results pave the way for conducting highly instrumented tests of melt-concrete interactions at prototypic temperatures to quantify the phenomena.

164 220

The experimental results were primarily thermocouple traces and gas samples. The temperature results indicate the initial concrete penetration was 2.0 to 2.5 cm/min. The outlet gas temperature was low enough throughout the test for instrumentation placed at the orifice to survive. The visually determined gas flow rates indicated a pulsing rather than a uniform flow rate. The gas samples indicate considerable amounts of H_2 and CO are present and that C may be released from the gas in particulate form.

Model Development

A preliminary comprehensive model of the melt-concrete interaction has been developed. The focus of the effort was to develop a reasonably complete model even though many effects are treated in a simplistic manner. The model has been provided to preliminary users.

1.2 Small-Scale Melt-Concrete Interaction Tests

(D. A. Powers)

1.2.1 Introduction

Experimental activities during the report period which yielded tangible results were confined to the fabrication and successful testing of an instrumentation tower for small-scale, prototypic temperature, melt/concrete interaction tests. Descriptions of this successful test constitute the majority of this section.

1.2.2 Experimental

The test, designated SSB-2, was conducted in a manner similar to that used in previous small-scale tests of this type.[1,2] The crucible was a rectangular block of calcareous concrete 10-13/16 x 10-13/16 x 22-5/8 inches with a cylindrical cavity 4-7/8 inches in diameter and 17-5/8 inches long. The crucible was fitted with a steel instrumentation tower whose design has been discussed previously.[2] The assembled fixture is shown in Figure 1.

The instrumentation tower used in this test satisfactorily served several purposes. The tower was sealed to the concrete crucible through a graphite compression

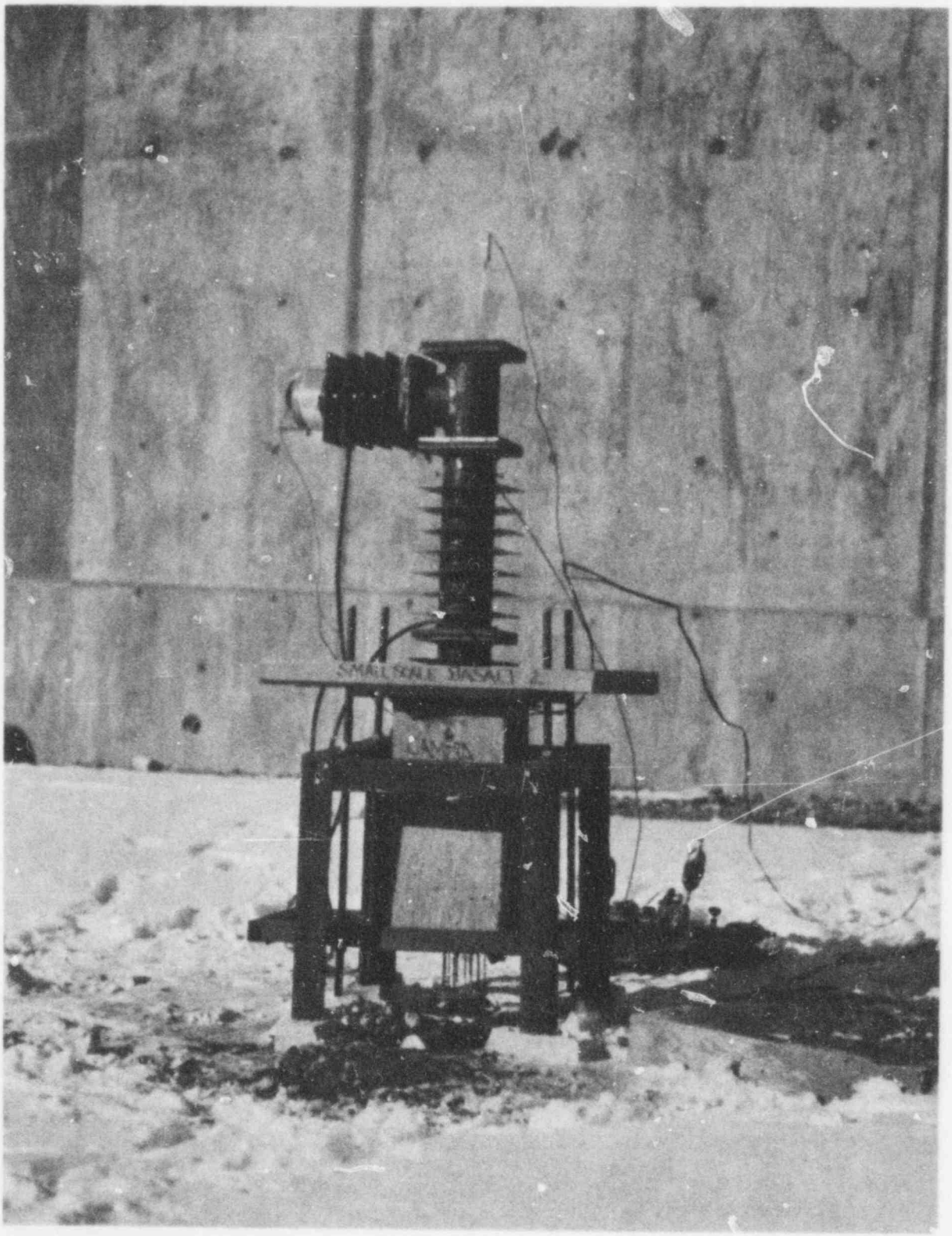

Figure 1. Assembled Test Fixture Used in Test SSB-2

seal[2] so that the thermitically generated melt was retained in the crucible. Gases evolved during the melt/concrete interaction were channeled to instrumentation in the tower. The massive baffle system within the tower cooled the evolved gases to temperature compatible with instrumentation in the tower.

Only limited diagnostic instrumentation was applied to this demonstration test. Thermocouples were embedded in the concrete in an arrangement that has been previously described.[1] Thermocouples were also located in the barrel of the tower and near the exit part of the tower. "Grab" samples of gases evolved from the melt/concrete interaction were abstracted from the tower using electrically actuated valves.[2] Color motion picture records of the test were made at 24 and 368 frames per second.

The metallothermic charge used to generate the test melt consisted of 10.86 kg of a 76.3 w/o Fe_3O_4, 23.7 w/o Al mixture.[1]

1.2.3 Results

1.2.3.1 Events of the Test

A tabulation of the major, macroscopically observable events in the test is shown in Table I. A compilation of photographs taken from the motion picture record of the test is shown in Figure 2.

Shortly after ignition of the charge, white smoke was emitted from the instrumentation tower. These emissions of what is believed to be aluminum oxide increased in intensity until they became sufficiently intense that the test fixture was occasionally obscured from view. The aerosol emission became dark brown to black in color 11 seconds after the start of the test. This dark aerosol consists of a variety of species including some carbon. This carbon may have come from the graphite seals within the instrumentation tower and at the tower-concrete interface. Posttest inspection of the test fixture produced little evidence of damage to the seals. The carbon may also be the result of chemical processes natural to the gas stream produced in the melt/concrete interaction. This second possibility is discussed below.

TABLE I

Events in the Test

Time (Seconds)	Description of the Event
0.0	Fuse ignition.
6.3	Charge ignition.
11.2	Emission of white aerosol from the instrumentation tower first detected.
22.1	Aerosol emissions darken.
25	First gas sample extracted.
31	TC8 begins to respond.
31.6	Flame ignited at the exit port of the instrumentation tower.
34	Second gas sample extracted.
40.2	TC8 fails.
41	Third gas sample extracted.
46	TC5 responds.
48	Fourth gas sample extracted.
50.5	Gas stream still ignited. Cameras depleted of film.
51	TC6 responds.
55	Fifth gas sample extracted.

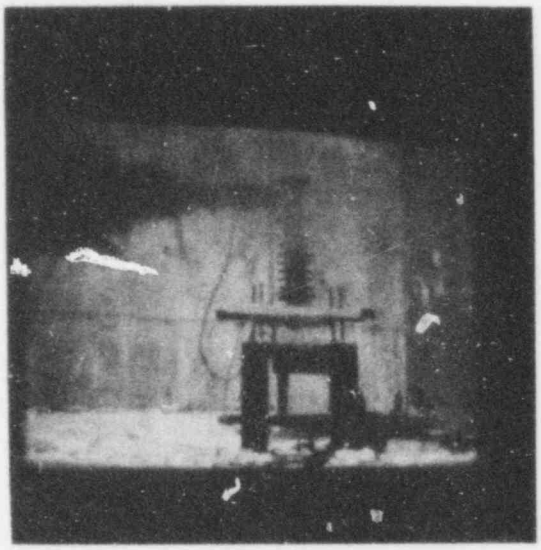

(a) White smoke emissions
Time = 12.0

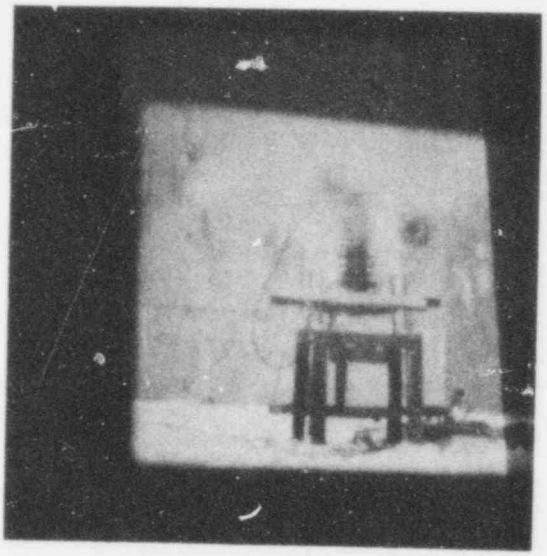

(b) Continued white smoke emissions
Time = 15.0

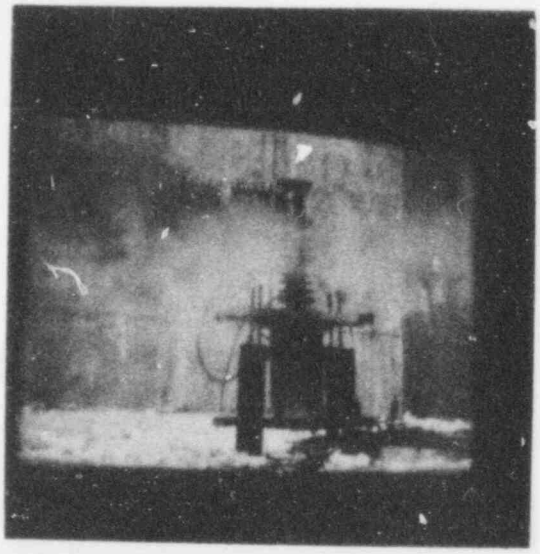

(c) Dark brown smoke emissions
from instrumentation tower
Time = 22.0

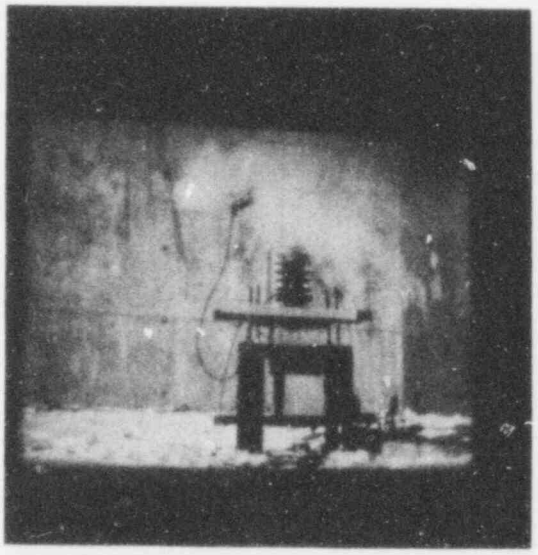

(d) Streaming brown smoke
emitted from tower
Time = 27.0

Figure 2. Photographs of Events from Test
(Times in seconds after fuse ignition)

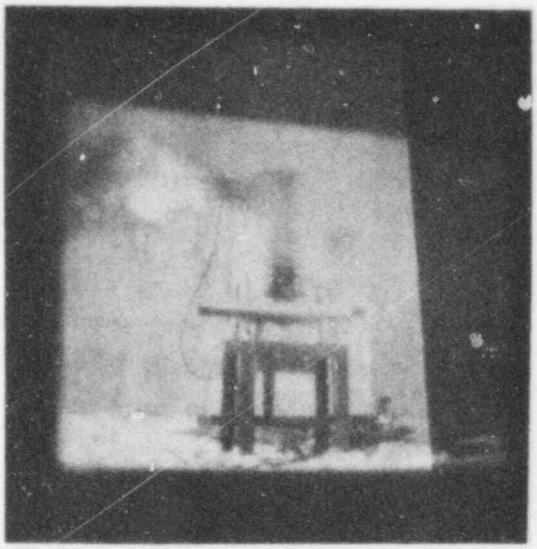

(e) Flame forms in exit gas stream
Time = 32.0

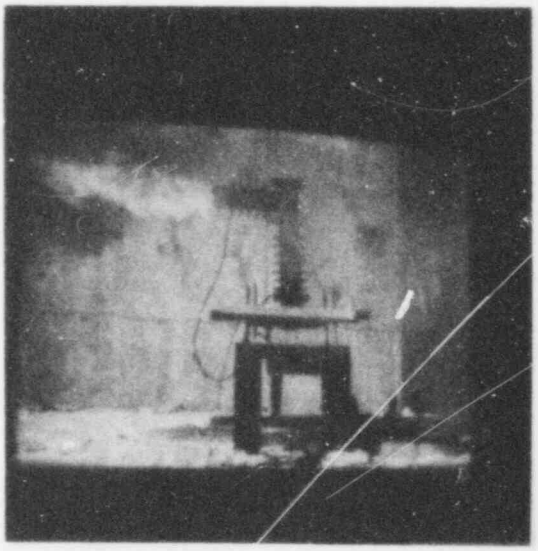

(f) Well developed flame stream exiting tower
Time = 38.0

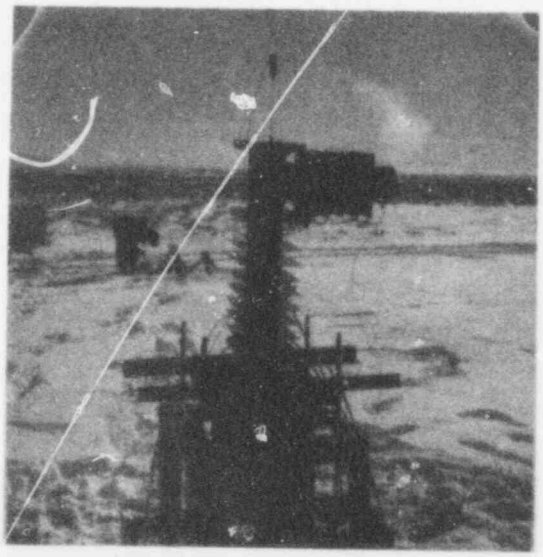

(g) Steam escaping from test fixture
Time = 360.0

Figure 2. (Cont'd.) Photographs of Events from Test
(Times in seconds after fuse ignition)

Flame appeared at the exit port of the tower 25.3 seconds after ignition of the metallothermic charge. Aerosol emissions from the tower waned substantially with the appearance of this flame. Careful inspection of the photographic records of the test suggests that ignition of the gases evolved in the test occurred within the gas stream and not at the port orifice (see Figure 3). The gas stream at the time of ignition is badly obscured by the evolved aerosol and the above observation may be in error. If accurate, it suggests that ignition may have been brought about by the aerosol once the gas stream had emerged into an environment where oxygen was available to sustain combustion. Homogeneous ignition of diffusional flames is an unlikely process.[3]

The flame jet from the test fixture eventually extended to a length of more than 3 feet. Its color at ignition was a very bright yellow. Ten to fifteen seconds later the flame was very pale and barely visible. The intensity of the flame declined smoothly during the test. Aerosol emission from the test fixture, on the other hand, exhibited the pulsating behavior observed in the previous small-scale tests.[1]

Accurate time estimates for the end of the flame emissions from the tower could not be made. For fully twenty minutes after the start of the test, steam escaped from the exit port. For an even longer time, liquid water dripped from the tower. Water also flowed from cracks in the concrete just as in previous small-scale tests.[1] Gurgling sounds, punctuated by mild popping sounds, could be heard emanating from the crucible.

1.2.3.2 Instrumental Results

Temperature data provided by thermocouples incorporated in the test fixture are shown in Figures 4 and 5. Thermocouples located near the gas sampling ports in the instrumentation tower barrel were destroyed quite early in the test. Consequently, no data, concerning the temperature of the evolved gas stream at the time "grab" samples were extracted, were obtained. Posttest inspection of these sensors showed that they had been fouled by molten metal.

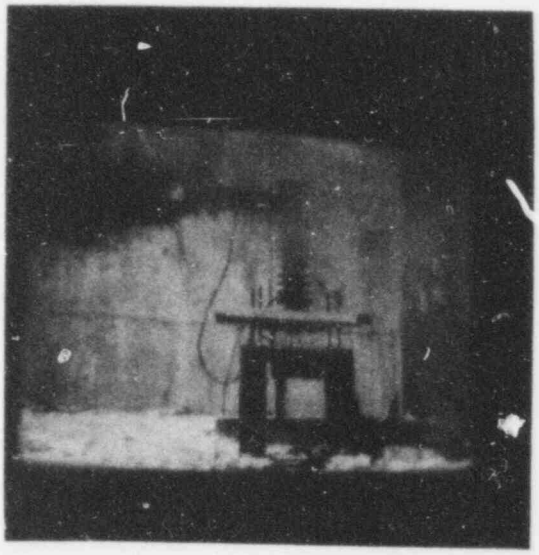

(a) First signs of incandescence in the gas stream
Time = 31.310

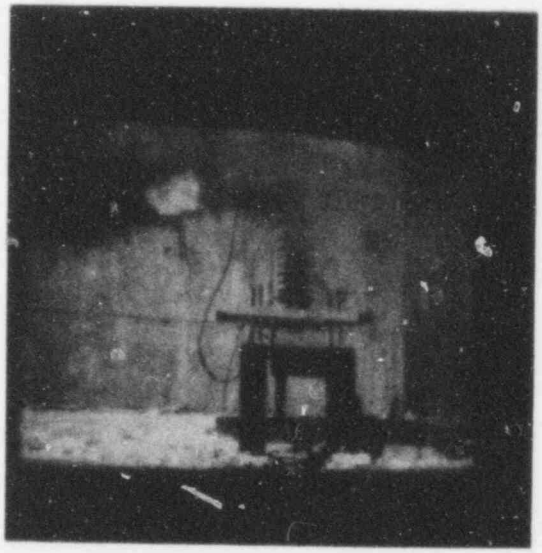

(b) Flame grows
Time = 31.613

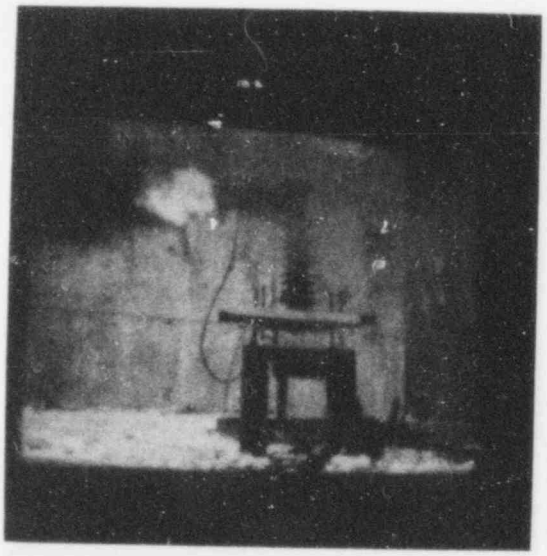

(c) Flame not yet in contact with the exit oriface of tower
Time = 31.616

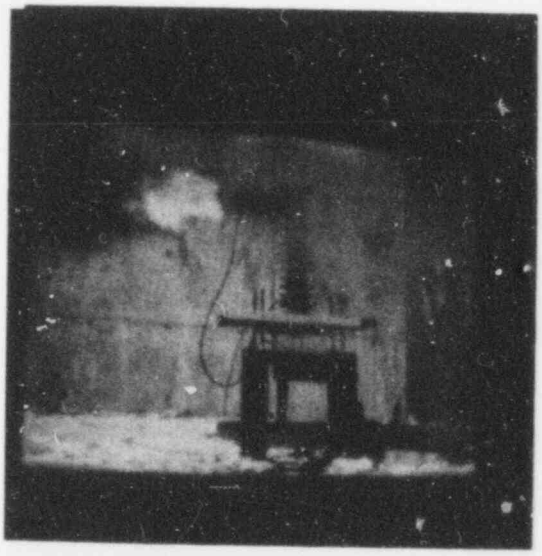

(d) Flame in contact with the metal structure
Time = 31.619

Figure 3. Flame Ignition in the Gas Stream
(Time in seconds after fuse ignition)

764 234

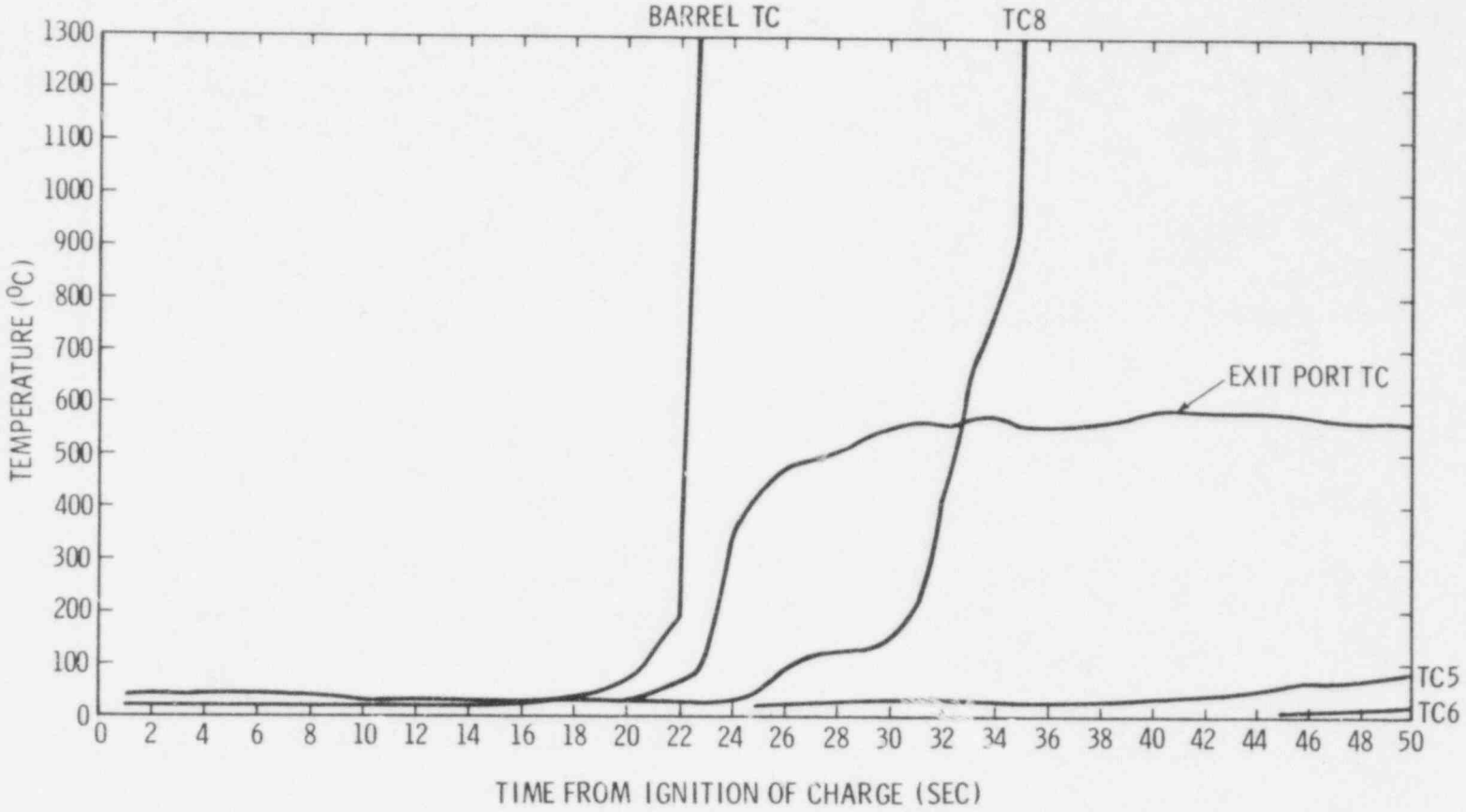

Figure 4. Temperature-Time Traces Reported by the Indicated Sensor in Test SSB-2

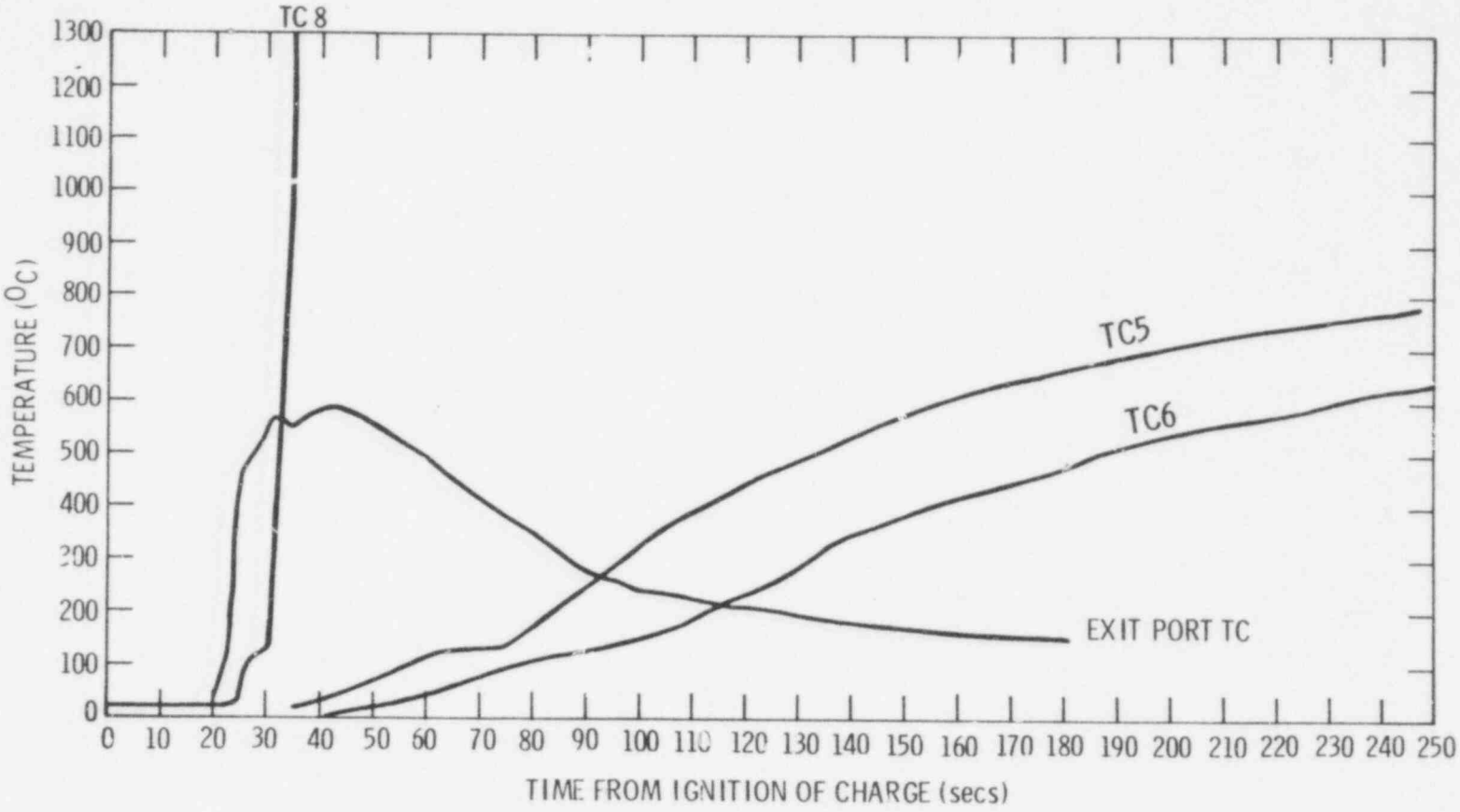

Figure 5. Temperature-Time Traces for Sensor Used in Test SSB-2

The thermocouple located near the exit port of the instrumentation tower recorded only mild temperatures. It began to respond approximately 18 seconds after charge ignition. It recorded a maximum temperature of 586°C at 42 seconds after the start of the interaction. Above ambient temperatures were still detected 5 minutes after the start of the test. The output from the sensor fluctuated during the test, perhaps as a result of fluctuating emissions from the site of the melt/concrete iterations, though other explanations could be advanced. Data from the exit port thermocouple show that the instrumentation tower satisfactorily cooled the evolved gas stream in the test to a temperature compatible with the instrumentation incorporated in this test and instrumentation planned in future tests.

Thermocouples TC8, TC6, and TC5 were located in the concrete 0.5, 2.28, and 1.78 cm below the crucible cavity, respectively. Sensor TC8 was failed 40.23 seconds after the start of the test. This failure indicates a melt penetration rate of 2.3 ± 0.5 cm/minute.

The overall behavior of the embedded thermocouples was qualitatively similar though on differing time scales. Each temperature-time curve begins with a sharp rise to 120° to 140° C. In this temperature range there is an arrest in the temperature rise. No further increase in temperature occurs for a period of 3 to 15 seconds. The temperature then begins to rise again, though additional small arrests in the temperature-time curves can be detected.

The arrests in the temperature histories reported by the embedded sensors TC6 and TC5 may be more clearly seen in plots of the time derivative of temperature versus temperature shown in Figure 6. Three distinct arrests are seen in these plots. They occur at 120°, 440°, and 650° C. Thermal arrests must certainly be due to thermally initiated endothermic reaction occurring in the vicinity of the junction of the thermocouple. The arrests cited above correspond closely to the major decomposition reactions in calcareous concrete - loss of evaporable water, loss of chemically constituted water and the loss of carbon dioxide.[1] The intensities of such thermal

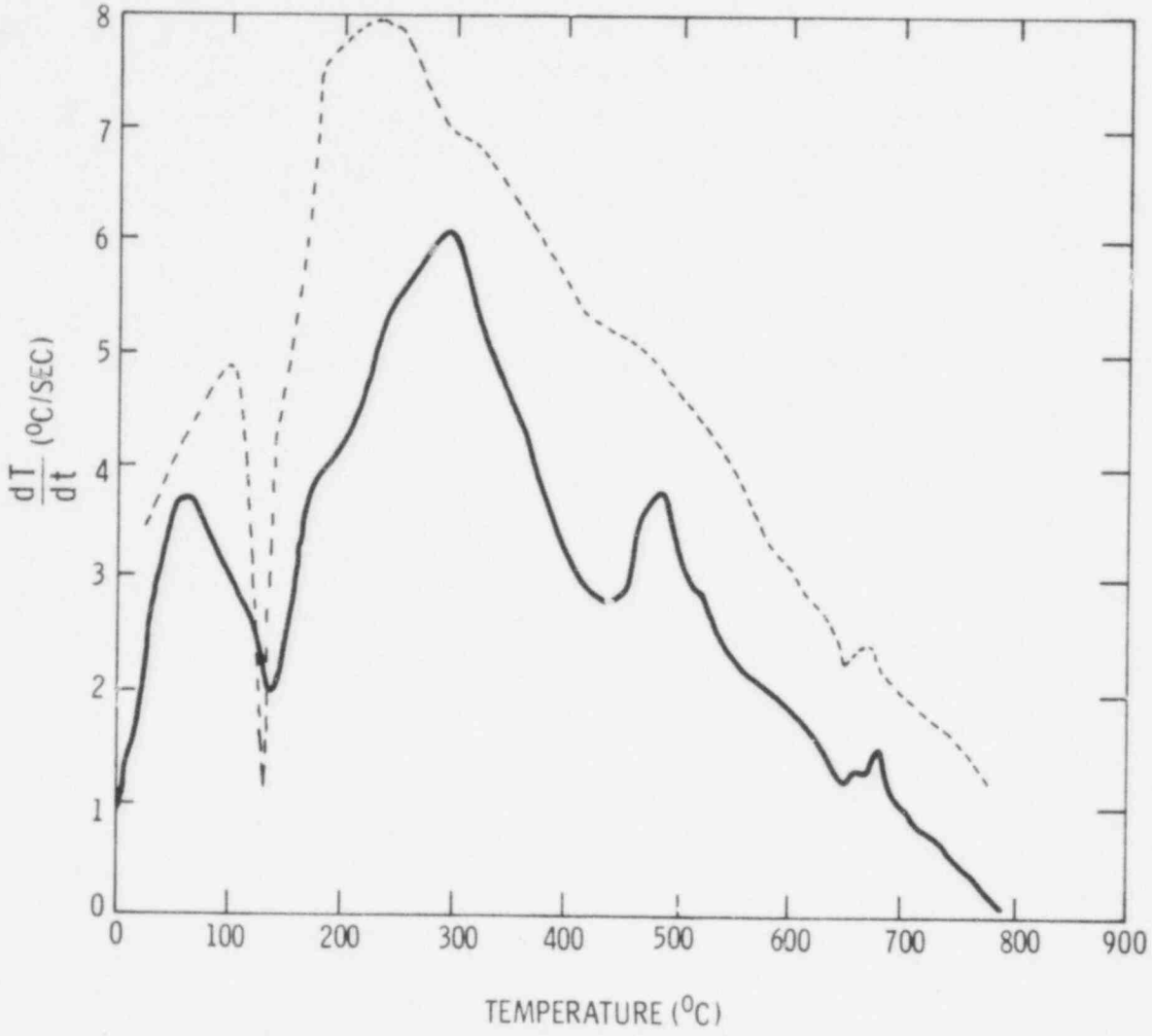

Figure 6. Time Derivative of Temperature versus Temperature Recorded by Sensors TC6 and TC5 in Test SSB-2

arrests are complex functions of the mass of reactive material surrounding the thermocouple junction, the rate of heating of the material, and the enthalpy the reaction events. The method of thermocouple location in the crucible used in the test SSB-2 assures that the junction is located within the cementituous material of the concrete. This would account for the relatively dramatic intensity of the arrest assigned to loss of evaporable water and the relatively weak intensity of the arrest assigned to the thermally initiated loss of carbon dioxide.

Thermocouples located in concrete are prone to errors due to the thermal conductivity mismatch between the sensor and the material. Errors of this type have recently been assessed[4] using a method proposed by Beck[5]. The difference between the temperature reported by the thermoelectric sensor and the temperature of the material, if the sensor were not present, is always negative and depends on the rate of concrete erosion as well as the absolute temperature. The expected measurement error for thermocouples of the type used in test SSB-2 at 227° and 1327° C is plotted against the concrete erosion rate in Figure 7. This figure shows that, at the failure temperature for erosion rates such as those encountered in this test, substantial errors in the absolute temperature measurements could be expected. However, since these errors are of the systematic variety, it ought to be possible, when more data on the melt/concrete interaction are available and after further analysis of that data, to correct thermocouple data for errors introduced by the presence of the thermocouple.

The extensive baffle system built into the instrumentation tower in test SSB-2 permitted acquisition of high quality "grab" samples from the gas stream evolved during the melt concrete interaction. These gas samples were analyzed by gas chromatography as previously described.[2] Results of the analysis, along with the analysis of a local air sample, are shown in Table II. The samples listed in this table are identified by the time in seconds after the start of the test on which they were acquired. As stated above gas temperature data at the time of sampling could not be obtained in this test.

The gas composition results demonstrate the highly reduced nature of gases evolved when molten steel interacts with concrete. The small amounts

764 239

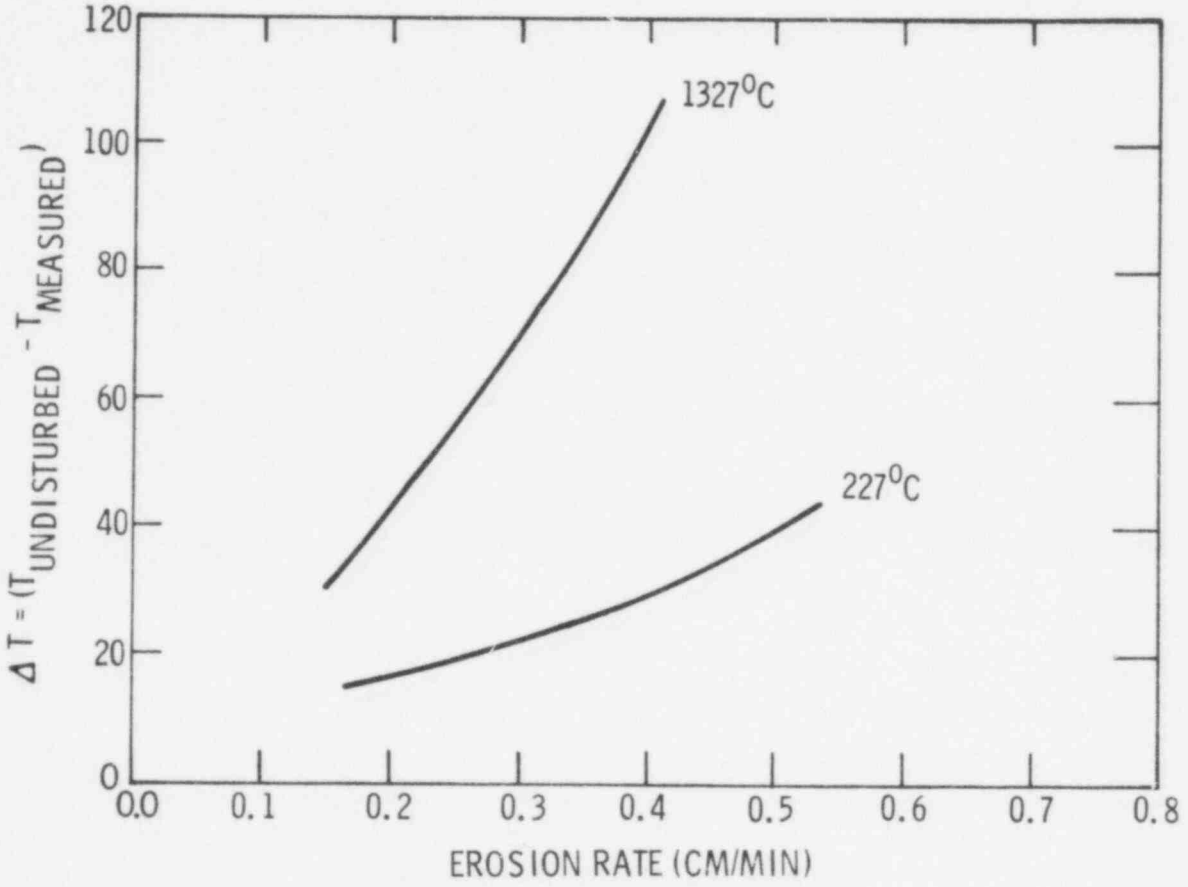

Figure 7. Estimated Measurement Error in Thermocouples Embedded in Concrete versus Concrete Erosion Rate

764 240

TABLE II

Gas Compositions

Gas Analysis From Test SSB-2
(Volume %)

Time[a] (Seconds)	H_2	N_2	O_2	Ar	CO	CH_4	CO_2	C_2H_4	H_2O
25	31.8	3.20	0.68	0.011	43.84	0.007	19.86	ND[b]	0.6
34	34.4	0.61	0.105	Tr[c]	28.84	0.044	35.25	ND	0.8
41	32.8	0.71	0.145	Tr[c]	51.0	0.009	14.86	0.005	0.52
48	35.4	3.91	0.97	0.015	49.27	0.028	9.71	0.023	0.65
55	38.0	16.95	4.24	0.060	38.3	0.025	2.19	0.015	0.2
"air"	ND[b]	76.7	22.07	0.64	ND[b]	ND[b]	0.024	ND[b]	0.2

(a) Time in seconds after fuse ignition.
(b) ND = none detected
(c) Tr = Trace

of nitrogen, argon, and oxygen present in the first three gas samples undoubtedly came from air trapped in the "dead" volume of the sampling apparatus. Similar gases in the fourth and fifth samples probably came from atmospheric gases diffusing back into the instrumentation tower at the low gas evolution rates near the end of the test. The O_2/N_2 ratio of the atmospheric impurities is low, relative to that in the local air (see Table III). This suggests that the atmospheric oxygen impurity may have reacted either with metals in the test fixtures or with the evolved gases.

The result of recomputing the composition of the gas samples, neglecting the Table III impurities, is shown in Table IV. The source of these gases is of course the thermally induced liberation of water and carbon dioxide from the concrete. These liberated gases percolate through the melt and are clearly reduced in the process. It is of interest, therefore, to compare the ratio of hydrogen and carbon in the gases to that present in the virgin concrete. The molar ratio H_2/C is plotted versus sampling time in Figure 8. The H_2/C ratio increases during the test. Forty seconds after the start of the test this ratio deviates substantially from that of the present in the original concrete ($H_2/C = 0.510$). It is probable that, as heat is transferred into the concrete, a point is reached at which the temperature rise created by this heat is sufficient to liberate water from the concrete but is not sufficient to decompose the more refractory limestone aggregate. Such a phenomenon would account for the increasing H_2/C ratio.

When gases are sampled at elevated temperatures, the possibility that these gases may react with the sampling apparatus exists. Further, if the temperature at which the gases are sampled is not the same as the temperature of the gases at the source, the measured gas compositions may not reflect the source gas composition accurately. The gas samples obtained in test SSB-2 have therefore been subjected to extensive thermodynamic analysis.[6,7] This analysis has been conducted in an effort to reconstruct the true gas compositions and derive the compositional history of the gases. Results of this analysis are briefly described below.

The computer code SPEDIS[7] was used to determine the "correspondence" temperature of each species in the five gas samples. The "correspondence"

TABLE III

Oxygen/Nitrogen Ratios in the Gas Samples

Sample	O_2/N_2 by Volume Ratio
"air"	0.2877
25	0.2128
34	0.1721
41	0.2042
48	0.2481
55	0.2501

764 243

TABLE IV

Gas Sample Compositions after Removal of Air Impurities

Sample Time (Seconds)	Volume %					
	H_2	CO	CH_4	CO_2	C_2H_4	H_2O
25	33.09	45.62	0.007	20.66	ND	0.62
34	34.63	29.03	0.044	35.49	ND	0.81
41	33.07	51.41	0.009	14.98	0.005	0.52
48	37.23	51.82	0.029	10.21	0.024	0.68
55	48.27	48.65	0.032	2.78	0.019	0.25

764 244

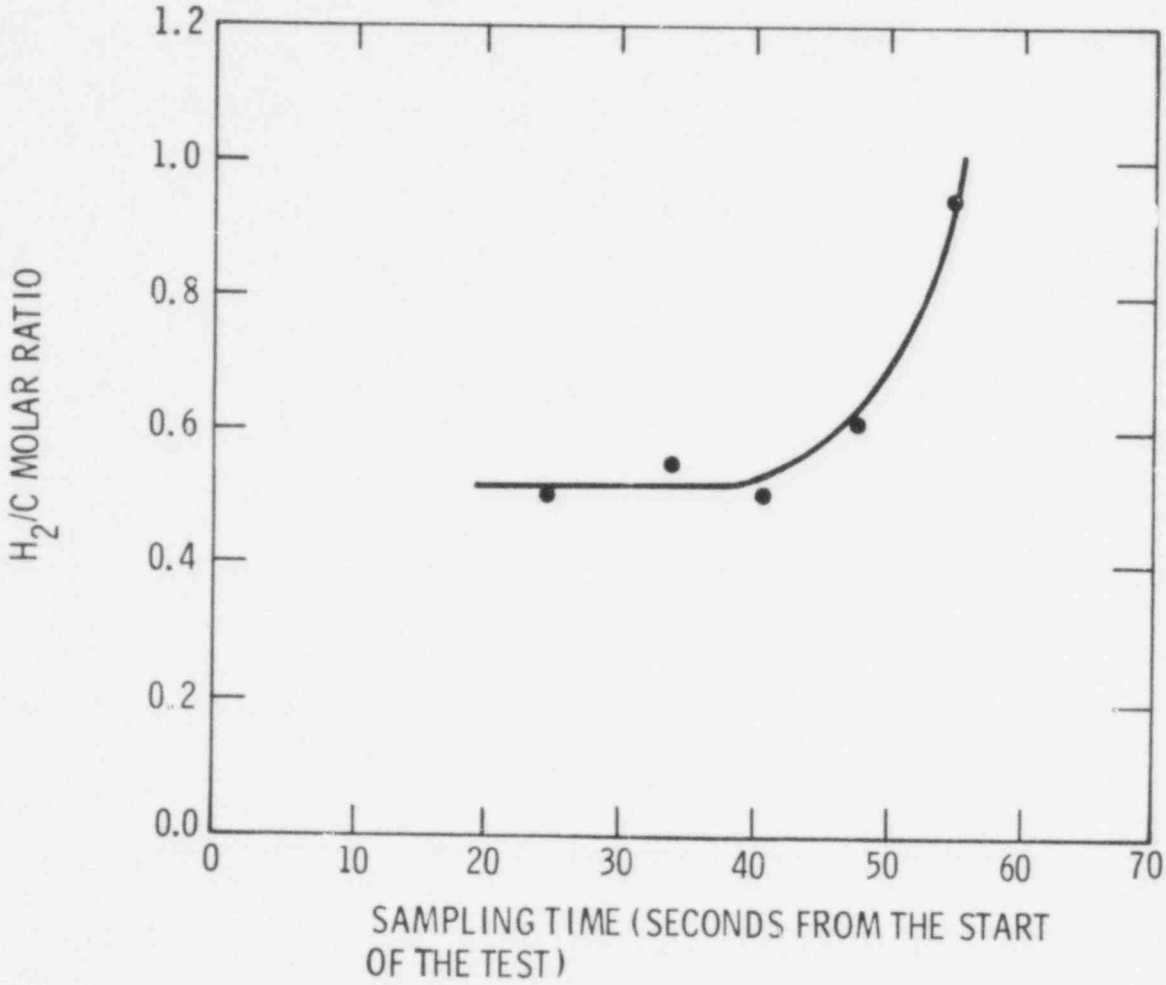

Figure 8. H_2/C Ratio of Gas Samples Acquired in Test SSB-2 versus the Time of Sample Acquisition

temperature is the temperature at which the calculated equilibrium concentration of a particular species in the mixture equals the observed concentration. "Correspondence" temperatures for the gas samples are shown in Table V. No "correspondence" temperature could be found for the hydrogen in the gas samples over the range of 100° to 1700° C. This fact and the extreme variability of the correspondence temperatures for other constituents of the gas samples indicate the mixtures are not at equilibrium.

The gas samples extracted from the test fixture 25 and 34 seconds after the start of the test have been subjected to further analysis in an effort to reconstitute the compositions of these samples when they were last at equilibrium. Inspection of the correspondence temperatures of the species in these two samples shows that CO_2 and CO must be very nearly at mutual equilibrium whereas H_2, H_2O, and CH_4 are severely de-equilibrated. Likely reactions which could lead to this de-equilibration are:

Metal-water

$$Fe + H_2O \rightleftharpoons FeO + H_2$$

Carbon deposition

$$CH_4(g) \rightleftharpoons C(s) + 2H_2(g)$$

Carbon and oxygen were therefore mathematically added to the gas mixture to form H_2O and CH_4 until a uniform correspondence temperature was found for the species in each mixture. The resulting compositions of the gas aliquots and their correspondence temperatures, which are also the temperatures at which the species in the samples were last at equilibrium, are shown in Table VI. The equilibrium temperatures are entirely consistent with the circumstances of test SSB-2. It is noteworthy that the carbon additions necessary to reconstitute the sample acquired at 25 seconds, and by implication the amount of carbon that must have been lost by the gas as it cooled, are of the same order of magnitude as aerosol emissions observed in previous small-scale tests.

164 240

TABLE V

Correspondence Temperature (^{o}C) for Gas Sample Constituents

Sample Time (Seconds)	Correspondence Temperatures (^{o}C)					
	H_2	CO	CH_4	CO_2	C_2H_4	H_2O
25	--	645	905	660	ND	440
34	--	600	780	610	ND	--
41	--	675	920	680	205	470
48	--	700	905	710	150	460
55	--	775	1000	780	100	275

TABLE VI

Last Equilibrium Composition of the Gas Mixtures

Time = 25 Seconds Sample

Species	Volume %	Correspondence Temp.
H_2	23.44	810
CO	45.65	810
CH_4	0.031	810
CO_2	20.68	810
H_2O	10.20	810

O_2 added = 0.7502 gram/liter C added = 0.0012 gram/liter

Time = 34 Seconds Sample

Species	Volume %	Correspondence Temp.
H_2	19.13	727
CO	29.03	727
CH_4	0.044	730
CO_2	35.49	727
H_2O	16.31	727

O_2 added = 1.17 gram/liter C added = <0.0001 gram/liter

764 240

The consistent nature of the preceding analysis may be demonstrated by examining the appropriate fugacity - temperature relationships. The oxygen fugacity - temperature curve for the assemblage Wüstite (W) - Iron (I) is shown in Figure 9. Curves (a) and (b) in this figure indicate the oxygen fugacity in the samples acquired at 25 and 34 seconds, respectively. Below ~ 600°C both curves (a) and (b) pass into the wüstite stability field. Either equilibrium cooling of the gases to room temperature or quenching the gases from their correspondence temperatures along paths q_{25} or q_{34} brings the gases into the Wüstite stability field. Once there, the gases would oxidize available iron, as hypothesized above, provided kinetic factors were favorable.

The carbon fugacity - temperature relationship for graphite in equilibrium with a carbonaceous gas is shown in Figure 10. Again, curves (a) and (b) denote the fugacity of carbon in the gas samples acquired 25 and 34 seconds after the start of the test, respectively. Below ~ 600°C the curves (a) and (b) pass into the graphite stability field. Consequently, either equilibrium cooling of the gas mixtures or quenching the gas mixtures from their respective correspondence temperatures (paths q_{25} and q_{34}) would place the gas samples in a situation where they would have to deposit solid carbon.

The closeness with which the oxygen fugacities of the two gas samples follow the oxygen fugacity over Wüstite in equilibrium with iron suggests the compositional histories of the gas samples may be estimated from the behavior of the W-I oxygen fugacity - temperature curve. Results of such extrapolations to temperatures of 900° to 1700° C are shown in Table VII.

These results indicate many interesting phenomena. Among them are:

(a) As the temperature increases, stability of carbon monoxide increases at the expense of cardon dioxide.

(b) The CO/CO_2 equilibrium disrupts the expected behavior of the H_2/H_2O equilibrium so that water becomes more stable at higher temperatures.

(c) As temperature is increased, the very active species atomic hydrogen (nascent hydrogen) becomes a more significant contributor to the gas composition.

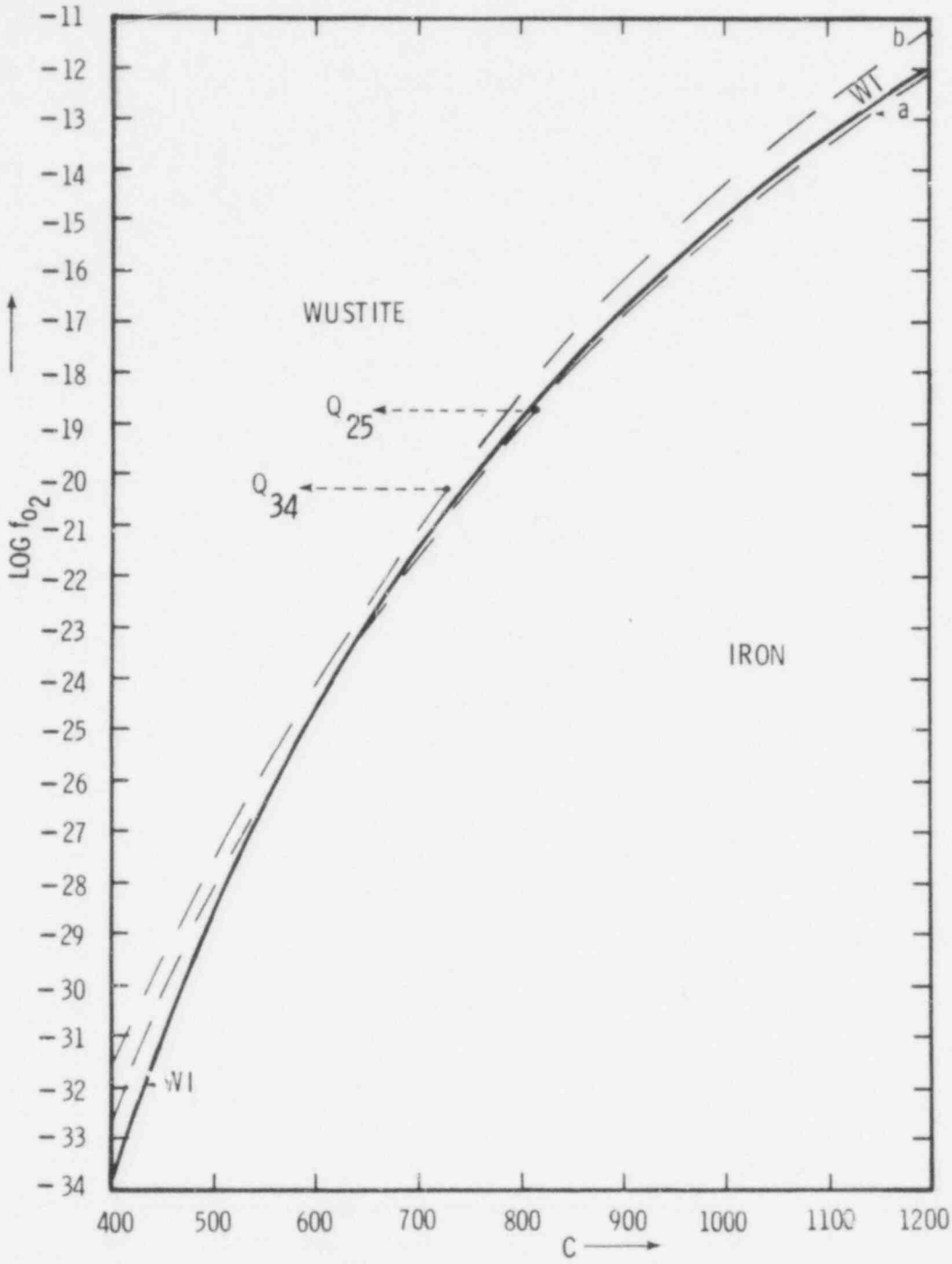

Figure 9. Oxygen Fugacity versus Temperature for Wustite in Equilibrium with Iron

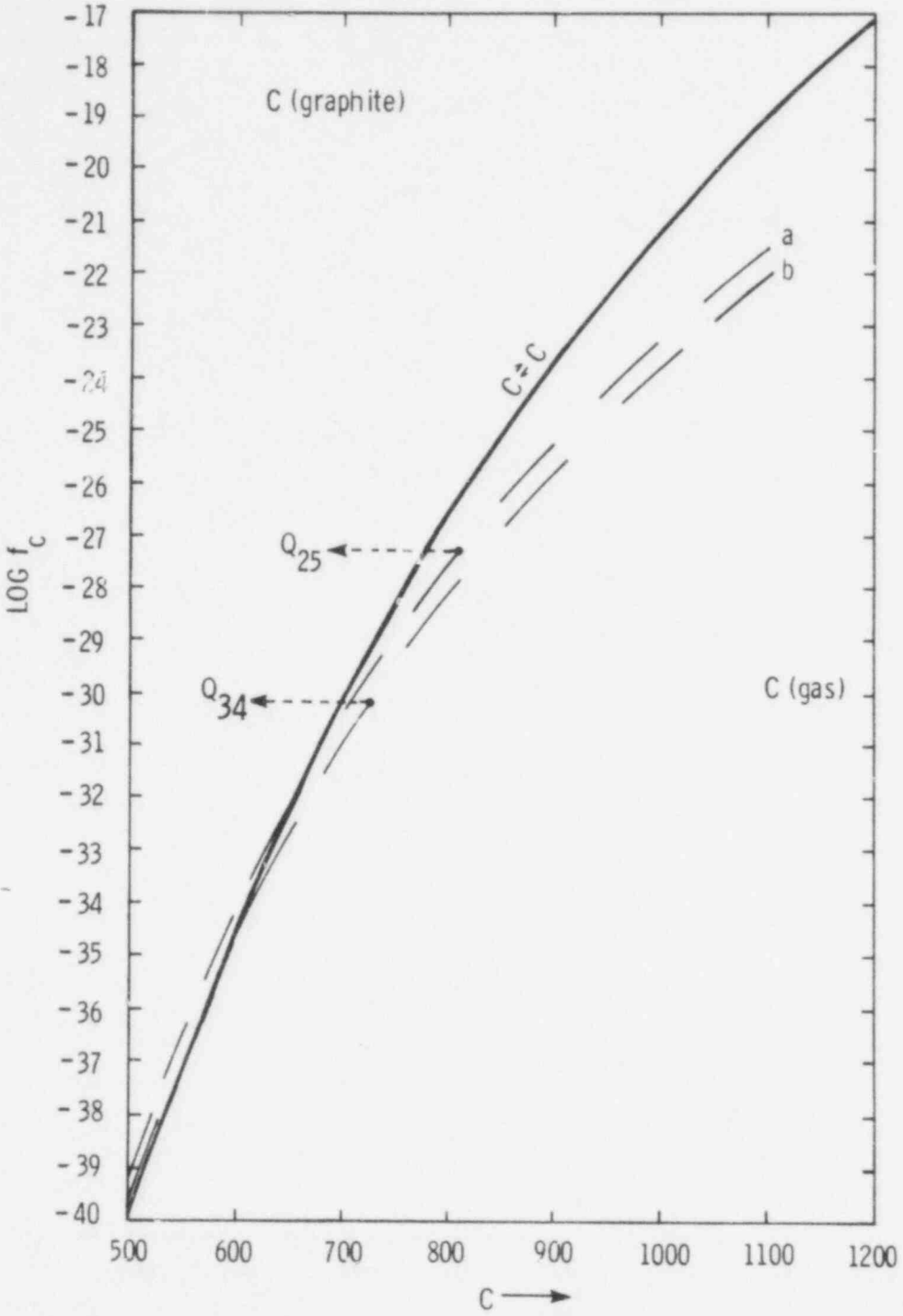

Figure 10. Fugacity of Carbon in a System of Graphite in Equilibrium with a Carbonaceous Gas verses Temperature

TABLE VII

Estimated Gas Compositions at Elevated Temperatures

Time = 25 Seconds Sample

Species	Gas Composition in Volume % at the Indicated Temperature (°C) 900	1100	1300	1500	1700
H_2	22.15	19.79	18.12	16.91	16.01
CO	47.01	49.38	51.05	52.24	53.11
CH_4	0.003	---	---	---	---
CO_2	19.31	16.94	15.27	14.07	13.18
H_2O	11.53	13.90	15.56	16.76	17.64
H	---	---	---	0.01	.05

Time = 34 Seconds Sample

Species	Gas Composition in Volume % at the Indicated Temperature (°C) 900	1100	1300	1500	1700
H_2	15.79	13.11	11.31	10.06	9.14
CO	32.50	35.18	36.98	38.23	39.12
CH_4	---	---	---	---	---
CO_2	32.0	29.32	27.53	26.27	25.37
H_2O	19.70	22.38	24.18	25.43	26.31
H	---	---	0.001	0.009	0.04

The currently available data base for the analysis of complex gas equilibria such as described above is limited to the temperature range of 100° to 1700° C. Efforts are now underway to extend this data base up to prototypic temperature (2600° to 3000° C) and also include data for condensible vapor species.

1.2.3.3 Posttest Analysis of the Test Fixture

Little posttest analysis of the test fixture was done during this report period. Disassembly of the instrumentation tower showed the slant baffles at the base of the tower were completely destroyed. Bristle baffles near the base of the tower were pierced. Other baffles within the tower baffle had sustained significant melting. The magnitude of this melting decreased with increasing distance from the hot zone in the crucible. Baffles in the side arm of the tower were badly rusted by the steam escaping from the fixture but were otherwise undamaged (see Figure 11).

The crucible itself bore an appearance quite similar to that of the crucible used in other tests. The crucible was cracked on 3 sides as shown in Figure 12. The surface to which the instrumentation tower was sealed was free of any blemishes indicative of venting through the seal.

The inner surface of the crucible cavity was coated with a pale green slag to a depth up to 1/2 inch. The diameter of the cavity had been expanded by nearly 1 inch. The slag pool at the base of the cavity was 3/4 to 1 inch thick. The metallic portion of the melt had solidified as a coherent mass. Its weight, 5.167 kg, was 86.2 percent of the weight calculated by assuming stoichiometric reaction of the melt-forming charge. The instrumentation tower obviously retained the melt and solid concrete decomposition products within the crucible in a completely satisfactory way.

When the metal slug was cut, it was found relatively free of gas pockets. A single slag inclusion approximately one-inch long and 1/16 inch thick could be seen in the cross-section of the metal slug.

The metal/concrete interface was identical to that observed in previous small-scale tests with calcareous concrete. It consisted of a thin, dark, incipient melt region. Below this layer were two distinct layers of thermally altered but not melted concrete.

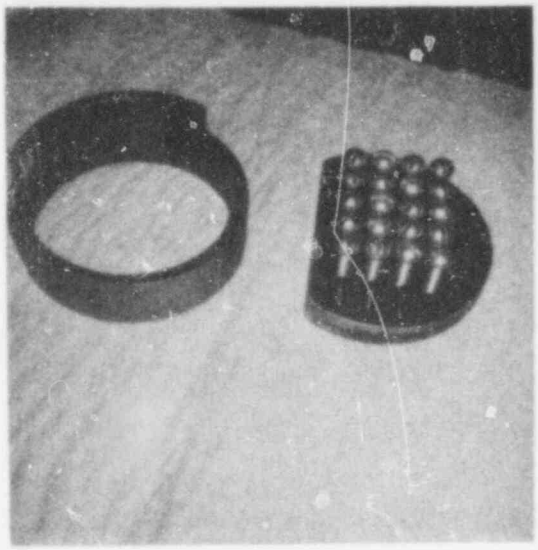

(a) Original baffle.

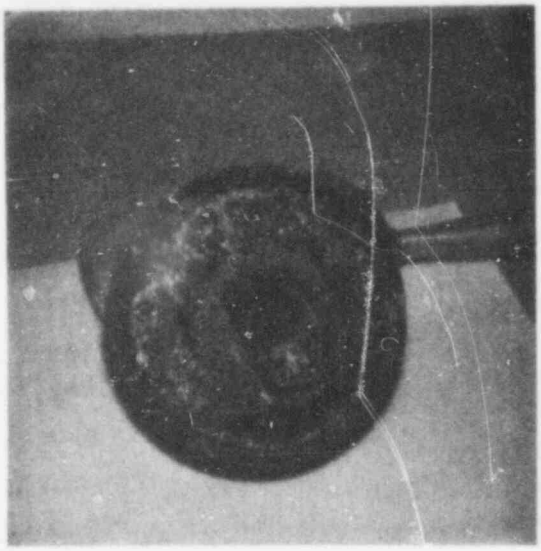

(b) Baffle from barrel of the tower near the tower/concrete interface.

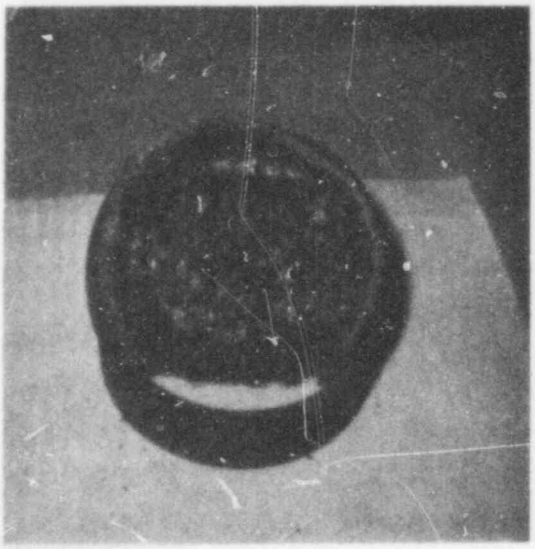

(c) Baffle from the mid-section of the tower.

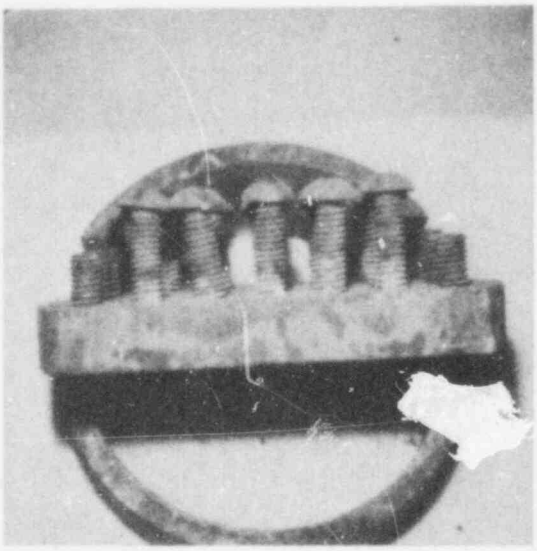

(d) Baffle from the Exit Port of the tower (some cold fingers on the baffle were bent when it was removed from the fixture).

Figure 11. Baffles from the Instrumentation Tower

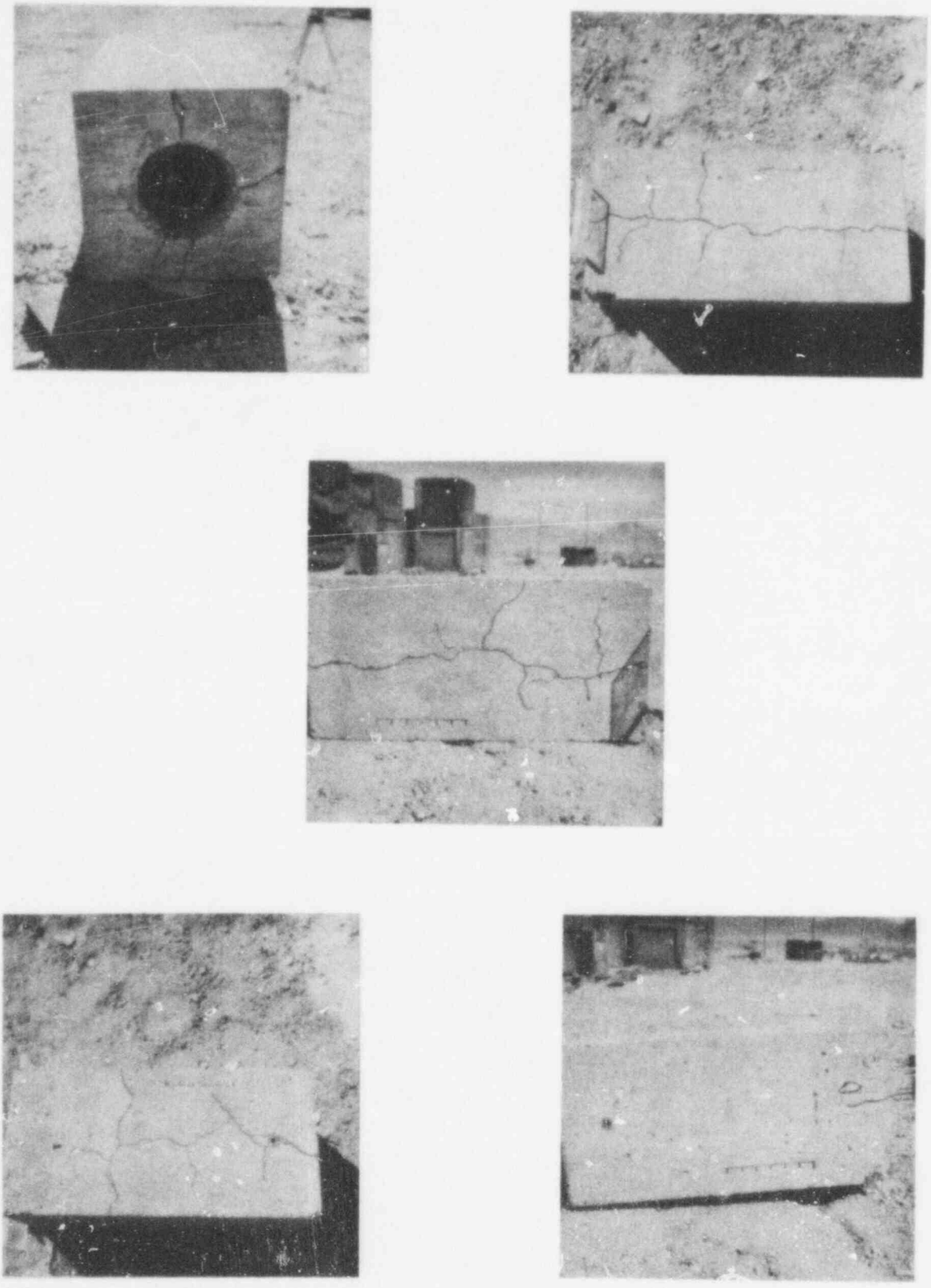

Figure 12. Crack Patterns in the Crucible.
Patterns have been accentuated in black for visibility.
The scale drawn on the side of each crucible is in inches.

1.2.4 Conclusions

A number of significant findings have come to light as a result of test SSB-2. Some of these are:

(a) The vigorous interaction that occurs when high-temperature melts contact concrete may be contained by an appropriately designed sealing arrangement.

(b) The gas stream evolved from the interacting melt/concrete system may be cooled sufficiently to permit real-time diagnostic investigation of the gas. Consequently phenomena which heretofore could only be subjectively described may be quantified.

(c) High quality "grab" samples may be taken from the evolved gas stream. Thermochemical analysis of the composition demonstrates the complex equilibria developed in the gas stream. These equilibria may have significant impact on questions of core meltdown phenomenology.

(d) Thermally induced gas generation from concrete occurs away from the melt/concrete interface and is the result of heat transfer into the concrete. As a result the composition of gases evolved during a melt/concrete interaction need not reflect the composition of vaporizable species in the concrete.

(e) Techniques are now available which allow correction of data acquired by thermocouples and gas sampling devices for errors induced by the presence of this instrumentation.

The above findings pave the way for conduct of highly instrumented tests of melt/concrete interactions with both steel and Corium-type melts at prototypic temperatures.

1.3 Core/Concrete Interaction Model

(W. B. Murfin)

1.3.1 Introduction

A mathematical model of core/concrete interaction is being formulated. This work has been divided into two phases: (a) a preliminary, approximate model to

be based on the earliest experimental results and (b) a more detailed and refined model to be formulated when more data become available.

This section describes the first phase of the modeling project and the initial stages of the second. Because a usable model was desired at the earliest possible time, many important and interesting phenomena could only be approximated. The model is therefore not predictive in the sense that fidelity to an actual core meltdown can be confidently expected. However, it is believed that the model can be used to describe major phenomena qualitatively and to determine the relative importance of many effects.

Two distinct layers are considered: a metallic layer and an oxidic layer. Each layer is considered to be homogeneous and isothermal, except for a thin boundary film. Heat transfer to the concrete is considered to take place across an interface consisting of two films, one being a mixture of solid and liquid concrete decomposition products and the other being the gaseous decomposition products. Cooling of the melt by radiative transfer from the upper surface and by gas blowing is also accounted for.

The model has been checked against experiments, and simulates test LSL-1 in the most important particulars. Sufficient empirical constants are included so that the fit can be improved as more experimental data become available.

The model has been incorporated into a computer code (INTER) which is currently operational.

1.3.2 Description of the Theoretical Model

A schematic conceptualization of the two layers is shown in Figure 13. Each layer (metal and oxide) is considered to be well mixed and isothermal in its interior as long as the layer is molten. Heat transfer from layer to layer takes place across a boundary layer or film whose thickness varies with the violence of mixing. The two main layers are assumed to be in intimate contact with each other, but there can be a vapor layer at the interface with the decomposing concrete. The thickness of the boundary layer can be different for each main layer; however, in each layer, it is uniform around the periphery of the layer. Heat is radiated to the containment, conducted into the concrete, and interchanged between layers.

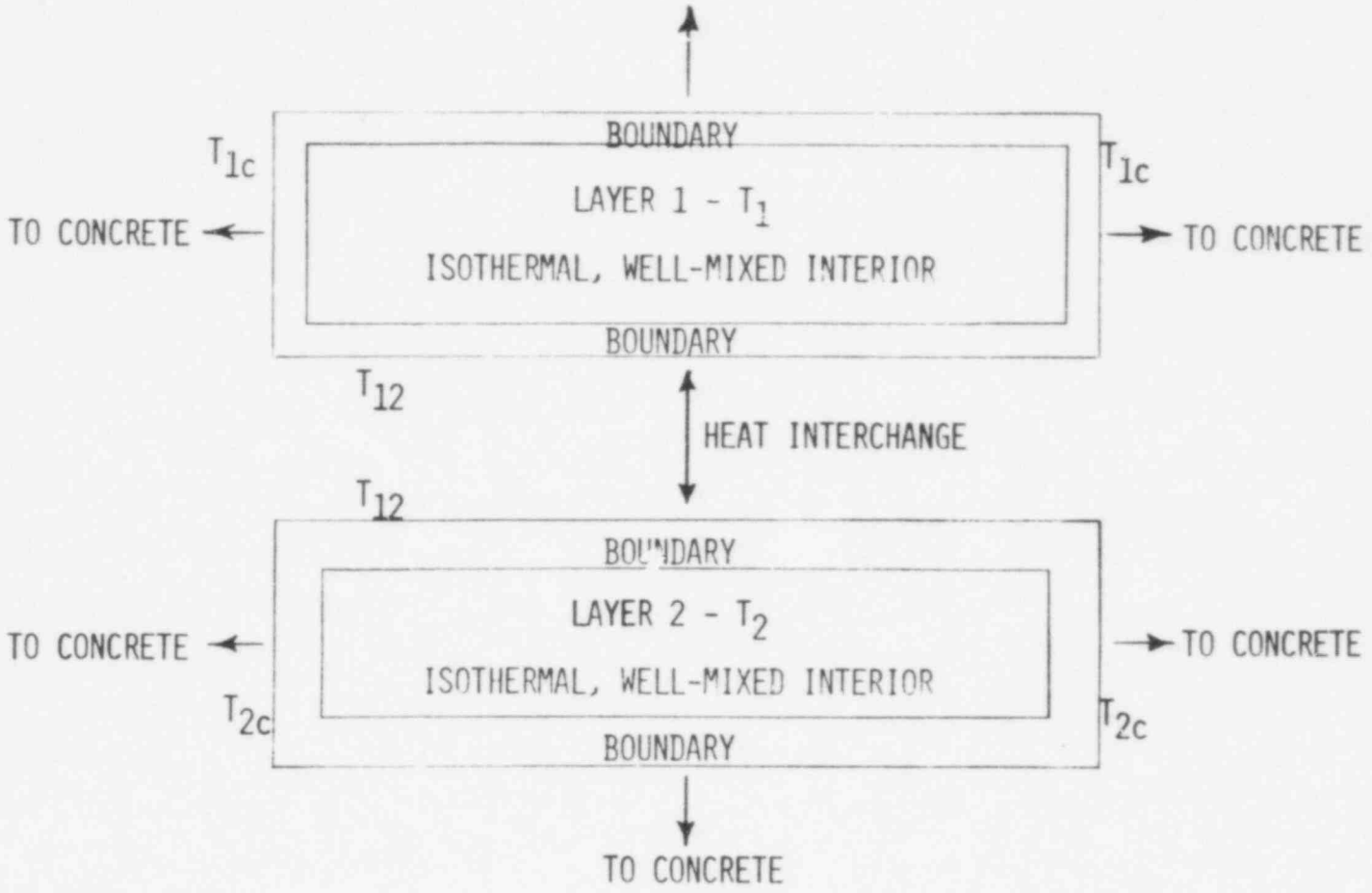

Figure 13: Schematic Conceptualization

The geometries considered are a hemispherical segment, a hemisphere intersected by a cylinder, or a flat cylinder.

Flows of material are shown in Figure 14. Material can be interchanged between layers. For example, iron oxides created by reaction of the steam with iron in the metallic part of the melt are assumed to be rapidly incorporated into the oxide layer. Solid or liquid decomposition products are assumed always to go promptly to the appropriate melt layer. However, gaseous products will not pass through the melt if the interface with the concrete is vertical.

Gas induced circulation cells are shown in Figure 15. In a normal cell, more gas passes through the outside of the melt and circulation follows the top drawing. However, if the lower layer is hotter than the upper layer, more gas flows through the center and the circulation direction can be reversed. Even if one layer is frozen, as shown in the lower sketches, a circulation cell would be expected in the other molten layer. As a general rule, it is to be expected that a circulation cell will be set up if (a) the material is molten and (b) there is appreciable gas flow. The intensity of the circulation (and hence the thickness of the boundary layer) will depend on the rate of gas flow. Other factors influencing the boundary layer thickness include melt viscosity and gas flow path; these factors are not dealt with in this simple model.

The temperature in the i-th layer is described by

$$\frac{d}{dt}\left(M_i C_{pi} T_i\right) = \frac{d}{dt} Q_i$$

$$i = 1,2 \text{ (metal or oxide)}$$

where

M_i = mass of i-th layer

C_{pi} = specific heat of i-th layer

T_i = temperature of i-th layer

$\frac{d}{dt} Q_i$ = net rate of heat added to i-th layer

t = time

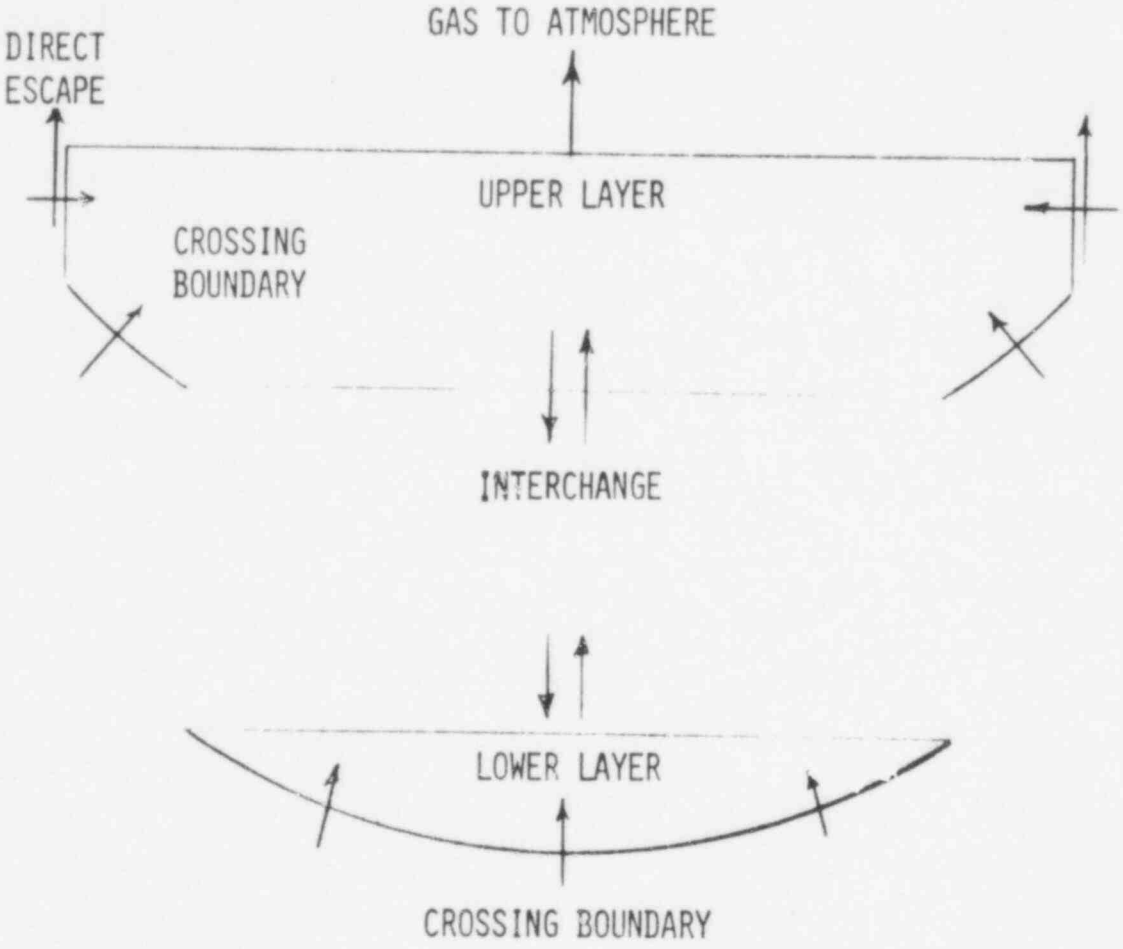

Figure 14. Flow of Material.

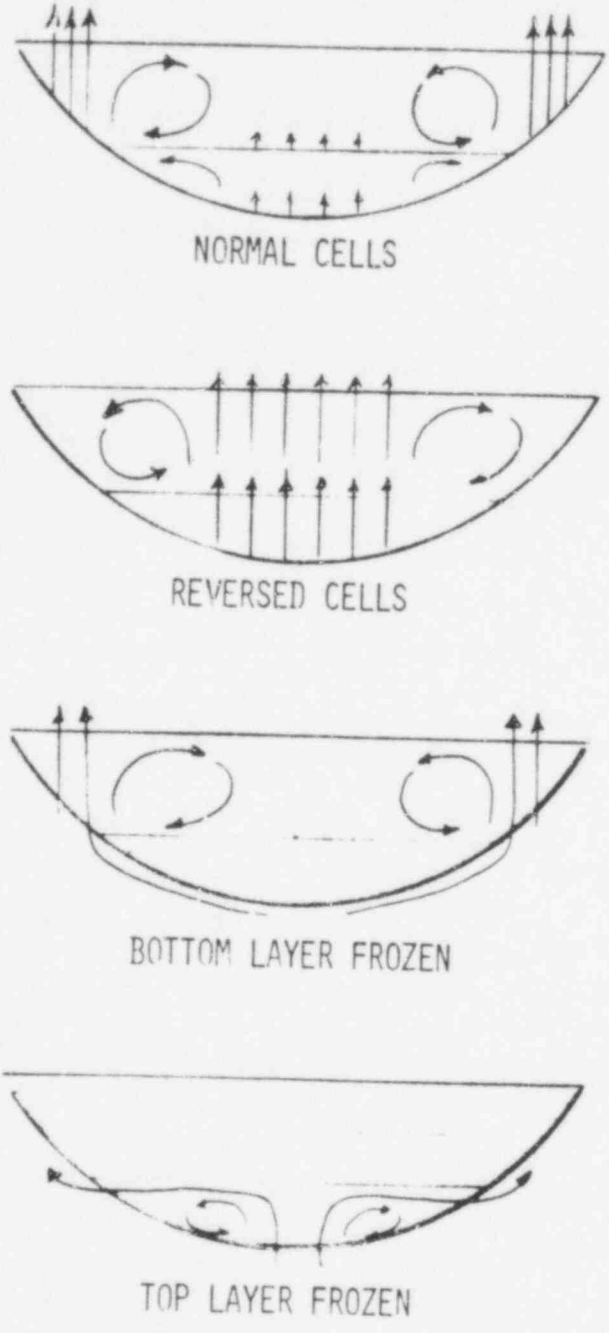

Figure 15. Gas Induced Circulation Cells

$$T_i^{n+1} \simeq \frac{T_i^n M_i^n}{M_i^{n+1}} + \frac{\dot{q}^n \Delta t}{M_i^{n+1} C_{pi}^n}$$

where the superscripts n and n+1 refer to the beginning and end of the time step. It has been found that the specific heats and heat rates are slowly varying quantities; and it is possible, with reasonably small error, to use these at the beginning of the time step only.

The rate of heat addition is the sum of internal decay heating, enthalpy of entering materials, internal reactions, and heat conducted from the other layer. This is reduced by radiation losses, enthalpy of material leaving, heat conducted to the concrete, heat lost to the other layer, and heat required to dissociate any concrete products not dissociated at the melt/concrete interface.

For all solid or liquid materials, the temperature at which materials leave is the temperature of the isothermal central region of the layer. However, it is possible for gases to transit the material so rapidly that they do not come into thermal equilibrium with the layer. An "equilibrium thickness" is assumed. The exit temperature is

$$T_{leav} = T^i - \exp(-x^i/x_r^i)(T^i - T_{ent})$$

where

T_{leav} = the exit temperature for gases

T^i = temperature of layer i

x^i = thickness of layer i

x_r^i = reference thickness of layer i

T_{ent} = the entrance temperature for gases

Density, conductivity, and specific heat as used in the model are functions of temperature. When a step change of properties occurs (at phase changes), the change is considered to take place over a few degrees interval, and the step is averaged over the interval.

764 262

The species considered are UO_2, ZrO_2, FeO, CaO, SiO_2, and ℓ_2O_3 in the oxide layer and Fe, Zr, Cr, and Ni in the metal layer. The material properties of each species are used to find a numerically averaged property for each layer.

The assumed temperature profile in the melt is shown in Figure 16. The interior of layer 1 is at a uniform temperature T_1, and the interior of layer 2 is at a uniform temperature T_2. There is a uniform gradient from T_1 to the surface temperature T_s and to the interface temperature T_{12} across the boundary of thickness δ_1. There is a uniform gradient from T_2 to the interface temperature T_{12} and to the temperature T_{2C}, on the melt side of the concrete interface. The boundary gradients are not necessarily equal.

The thickness of the boundary layer is assumed to grow at a rate

$$\frac{d\delta_i}{dt} = \frac{0.72\alpha_i}{\delta_i}$$

where α_i is the thermal diffusivity. This allows the boundary layer to grow at a reasonable rate when the material is frozen. However, when the layer is molten, various constraints always govern, so that the thickness is more appropriate for a gas driven circulation cell.

The melt/concrete interface is schematically depicted in Figure 17.

An estimate of the temperature on the concrete side of the interface is given by

$$T_{ic}{}^{T} = \frac{K_m \delta_c h_i T_m / R_c^2 + \left(K_c \delta_m h_i / R_m^2 + K_c K_m / R_i^2\right) T_c}{K_m \delta_c h_i / R_c^2 + K_c \delta_m h_i / R_m^2 + K_c K_m / R_i^2}$$

The trial temperature, $T_{ic}{}^{T}$, is compared with the decomposition temperature of $Ca(OH)_2$, T_{DC}, and the temperature for vaporizing free water, T_W. The actual temperature is set as follows:

$$T_{ic} = T_{ic}{}^{T} \left(T_{ic}{}^{T} < T_W\right)$$

$$T_{ic} = T_W \left(T_W < T_{ic}{}^{T} < T_{DC}\right)$$

$$T_{ic} = T_{DC} \left(T_{DC} < T_{ic}{}^{T}\right)$$

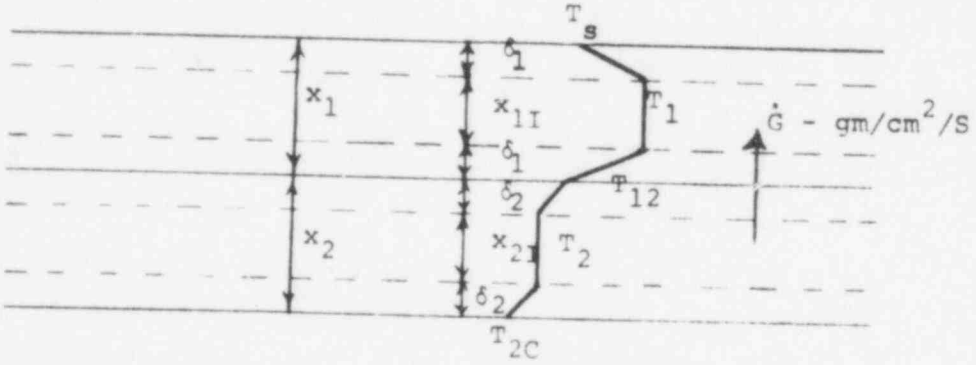

Figure 16. Temperature Profiles in Circulating Material

764 264

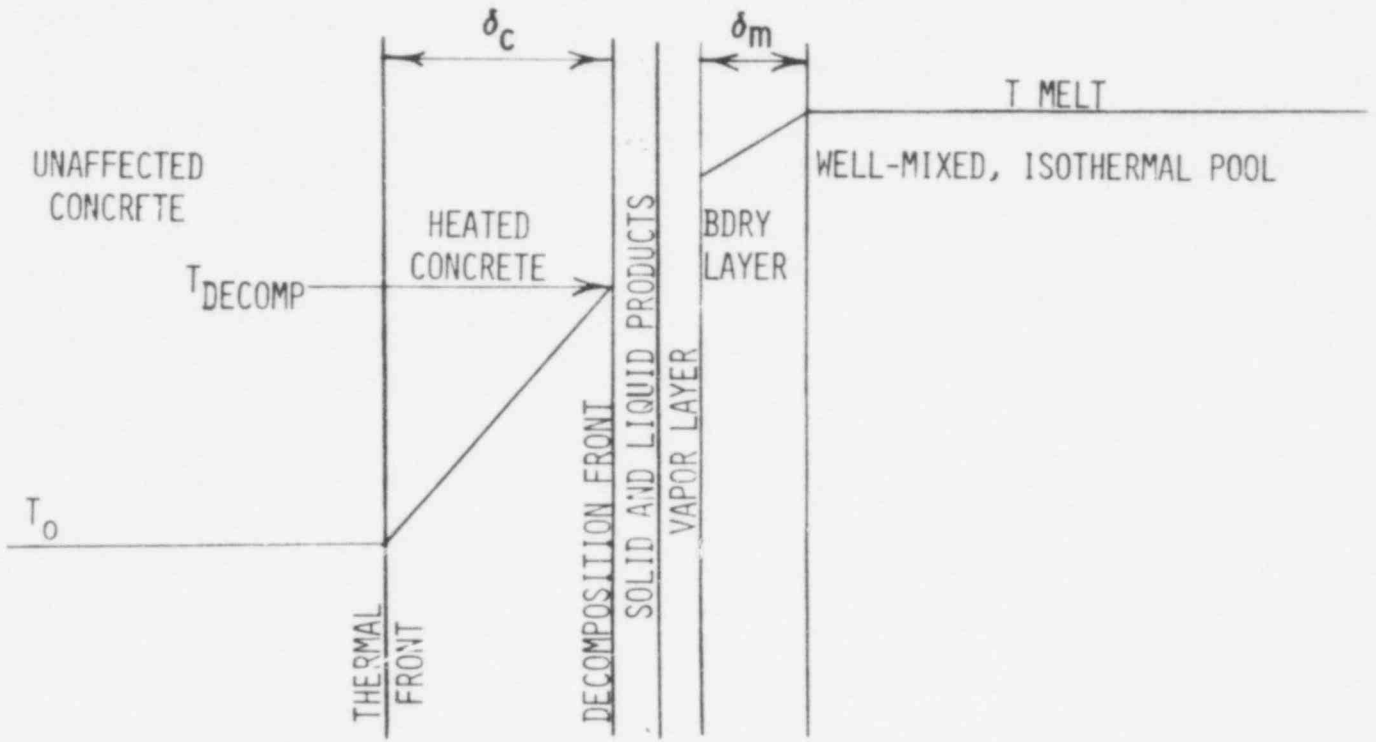

Figure 17. Interface Between Melt and Concrete

The temperature T_{im}, on the melt side of the decomposing interface, is calculated by

$$T_{im} = \frac{R_m^2 K_m T_m + R_i^2 h_i \delta_m T_{ic}}{R_m^2 K_m + R_i^2 h_i \delta_m}$$

where

K_m = thermal conductivity of melt

T_m = temperature of melt

h_i = interface heat transfer coefficient

δ_m = thickness of thermal boundary layer in melt

R_m and R_i are radii as shown in Figure 16.

The rate of recession, $\dot{x}$ is

$$\dot{x} = \frac{R_i^2 \delta_c h_i (T_{im} - T_{ic}) - R_c^2 k_c (T_{ic} - T_c)}{q_{CD} \rho_c R_i^2 \delta_c}$$

where

δ_c = "thermal penetration distance" in the concrete

T_c = initial temperature of the concrete

q_{CD} = heat of decomposition of the concrete

ρ_c = density of concrete

and other symbols are explained in the previous equation.

If $T_{ic} = T_{CD}$, the recession rate represents the rate at which the decomposition front moves into the concrete. If $T_{ic} = T_W$, decomposition is not taking place, and x is the velocity with which the water vaporization

front is moving into the concrete. If $T_{ic} < T_W$, there is no surface recession or water evaporation and this computation is bypassed.

The vaporization of free water does not indicate decomposition of the concrete. However it is assumed that dissociation of the calcium hydroxide will crumble the matrix. Even if the remaining constituents do not melt or dissociate, they will be absorbed into the melt. The dissociation temperature of calcium hydroxide is lower than the dissociation temperature of calcite or the melting point of silica; therefore, it is only necessary to determine whether the calcium hydroxide will dissociate to determine whether decomposition occurs. If the temperature T_{CaCO_3} is less than the interface temperature, calcite will also be decomposed in the interface. If the melting point of silica is less than T_{im}, silica will be melted in the interface. It is assumed that alumina can be released but not melted before incorporation into the melt.

In reality the oxidic constituents of concrete decomposition are mutually soluble. It would be more realistic to consider a liquid solution leaving the interface. Unfortunately, the problem of determining the melt temperature and properties introduces excessive complication.

Because of the probable complexity of material flow paths, some simplifications have been required. The following arbitrary rules are applied:

(a) All oxides are promptly transmitted directly to the oxide layer.
(b) All metals are promptly transmitted directly to the metal layer.
(c) Gases entering a layer leave the layer in the same time step.
(d) Gases released at a vertical interface flow directly to the atmosphere, without transitting the melt.
(e) Gases released at a nonvertical interface flow through the molten melt layers.
(f) Gases bypass frozen layers.
(g) Gases bypass any layer if at least 5 cm of the layer boundary is below the freezing temperature of the layer.

A continuous check is made on the relative average densities of the metal and oxide layers, and the more dense layer is always considered to be underneath.

The reactions considered in the core melt are

$$Fe + H_2O \rightarrow FeO + H_2$$

$$Fe + CO_2 \rightarrow FeO + CO$$

$$Zr + 2H_2O \rightarrow ZrO_2 + 2H_2$$

$$Zr + 2FeO \rightarrow ZrO_2 + 2Fe$$

The first three reactions are assumed to be limited by the mass of gases available, i.e., that all of the CO_2 and H_2O are reacted. This assumption is based on the experimentally observed fact that, when concrete is attacked by a few centimeters of molten steel, the gases appear to react completely. It is assumed that the reactions can be rate-limited if the mass rate-of-flow is large or the residence time is short.

The fourth reaction listed should be very rapid, provided that both reactants (FeO and Zr) are in intimate contact. However, the reaction will be limited by the rate at which circulation brings the reactants together at the metal/oxide interface. The rate of this reaction could have been made a function of gas flow, because the gases are the primary mechanism for circulation in the melt. However, this is believed to be an unnecessary complication; the effect desired is simply that the metallic zirconium be rapidly depleted. As a compromise, it is assumed that this reaction would proceed with a time constant of 300 seconds.

The interface heat transfer coefficients have been chosen to match, as nearly as possible, the metal and oxide cooling curves and total recession in test LSL-1. The boundary layer thicknesses have been chosen to allow oxide and metal temperatures to differ by a few hundred degrees when both materials are molten, as has been experimentally observed.

1.3.3 General Discussion

The model presented is to some extent based on conjecture. It is believed that the assumptions are reasonable, but certainly there is no proof of completeness or accuracy. It is also believed little can be done to improve these conditions until more experimental evidence is received. It is heartening to note, however, that the most realistic experiments can be reasonably well simulated.

Because of the number of assumptions and estimates, it should not be supposed that the model can "predict" such critical variables as the time of containment melt-through. The model can best be utilized to determine the general effect of changing parameters on the outcome of the meltdown process. For example, the effect of changing concrete composition on the gases evolved can be estimated, but one should not suppose that the model will accurately predict the time of containment overpressure failure for any specific set of circumstances. The model could be a useful tool in a sensitivity study to explore the importance of various parameters.

2. Steam Explosion Phenomena

(L. S. Nelson and L. D. Buxton)

2.1 Summary

A summary of the primary accomplishments during this quarter is given below:

(a) Several improvements to the steam explosion triggering experiment apparatus have greatly increased the experimental capability. These improvements include the installation of a greater capacity power supply to allow larger melt fractions, some modifications to the interaction chamber which improve its performance, and the augmentation of the flash x-ray apparatus to provide three separate images instead of the previous single image per experiment.

(b) Characterization of bridgewire-generated pressure transients was continued with 22 experiments. The nature of the bridgewire pulses and their propagation through the water-filled chamber have been studied.

(c) Gas analyses have been performed on two lots of stainless steel, before and after melting, in different atmospheres, and with and without flooding with water.

(d) Eleven tests to explore the effect of the pressure transient generating techniques on a non-interacting liquid metal have been performed in a simulated chamber in which mercury globules were exposed to detonator and bridgewire-generated pulses while submerged in water. Flash x-ray imaging and high-speed photography have indicated that normally the bridgewire-generated pulses produce only modest deformations of the mercury globules. The detonator generated pulses produced some mercury fragmentation; however, the observed fragmentation was milder than most which have been encountered when a high-temperature melt interacting with water is exposed to a detonator or bridgewire-generated pulse.

(e) Twelve experiments have been performed with the new power supply in which arc-melted stainless steel samples have been flooded with water and exposed to pressure transients. Some fragmentation occurred but

no return pressurizations were detected except for one experiment where a detonator was used for the pressure transient.

(f) In four experiments, samples of a "metallic" Corium-E simulant were melted with the new power supply. Because multi-phase liquids and solids were formed, no floodings were attempted. Some electron microprobe studies have been carried out on the solidified materials.

(g) Eight samples of an "oxidic" Corium-E simulant have been melted with the new power supply, seven of which were flooded with water and one which was frozen in argon. When applied pulses were used, extensive fragmentation occurred and pressure pulses with magnitudes of at least 7 bars were generated by the interaction. Electron microprobe studies were performed on the sample solidified in argon.

2.2 Experimental Apparatus

Experimental techniques improved significantly this quarter, mainly due to the installation of the new arc power supply. This unit, a controlled current Miller Type SR-1000-A1 power supply, employs a saturable core reactor which has been arranged for Variac control. The typical current drawn from the unit in a triggering experiment is 200 A at 60 V. Consequently, this unit provides roughly a four-fold improvement in power over the controlled potential Miller Type CP-3 power supply which typically delivered 100 A at 31 V. With the new power supply it is possible to prepare larger amounts of melt with shorter melting times; it is also possible to control the power during the arc melting procedure.

Some modifications to the interaction chamber have also improved our experimental capabilities. These include:

(a) Moving the flushing gas inlet from the top of the inner chamber to the base to allow upward, one-directional flushing of the arc melting gases;

(b) The use of sprayed alumina arc-electrode insulation instead of the fragile ceramic sleeves which were used previously; and

(c) Relocating the sleeve retraction springs from within the arc-chamber into extended cylindrical housings above the arc-chamber to prevent thermal failure of the springs.

2.3 Instrumentation and Diagnostics

2.3.1 Pressure Transient Characterization

This work is a continuation of the bridgewire generated pressure transient measurements started in the previous quarter.[9] Twenty-two characterization experiments were performed this quarter in which bridgewires submerged in 1.5 liters of water were fired in the interaction chamber (sleeve retracted, no melt on the hearth). Various capacitor charging voltages up to 3 kV were used to fire the bridgewires. Some mapping of the pressure pulse intensity within the water phase was carried out through use of transducers placed as in actual triggering experiments. It was found that, under apparently identical conditions, both the magnitude of the generated transient and the shape of the transient will vary somewhat from experiment to experiment. Also, the bridgewire produced pulses, as measured by an additional transducer in the water just above the hearth, were found to be tens of bars in amplitude and 25 to 50 microseconds wide in these experiments. Figure 18 shows a plot of the peak pressures seen by this additional transducer versus capacitor charging voltage. Care should be taken in extrapolating these data to the actual triggering experiments since two-phase effects will be present in the triggering experiments.

2.3.2 Three-flash X-ray Imaging

During this quarter, two flash x-ray pulser units were added to the system which had been in use previously. This completes the desired layout shown originally in Figure 2.2.2 of SAND75-0362.[10] This final array consists of three 300 keV pulsers spaced 45 degrees apart in the horizontal plane. This permits the recording of three 90-nanosecond exposure time x-ray images with each exposure at essentially any desired time delay. It should be noted that because of the large size of the pulsers it is not possible to make the three images superimposable.

In the steam explosion triggering experiments, the flash x-ray units have been discharged at delay intervals measured from the firing of the bridgewire or detonator. Two delay patterns have been used, one with pulsers 1, 2 and 3 delayed 2, 5, and 20 milliseconds, respectively, and the other with these pulsers delayed 2, 3.5, and 5 milliseconds. The new flash x-ray capability has provided excellent sequential imaging and time repeatability.

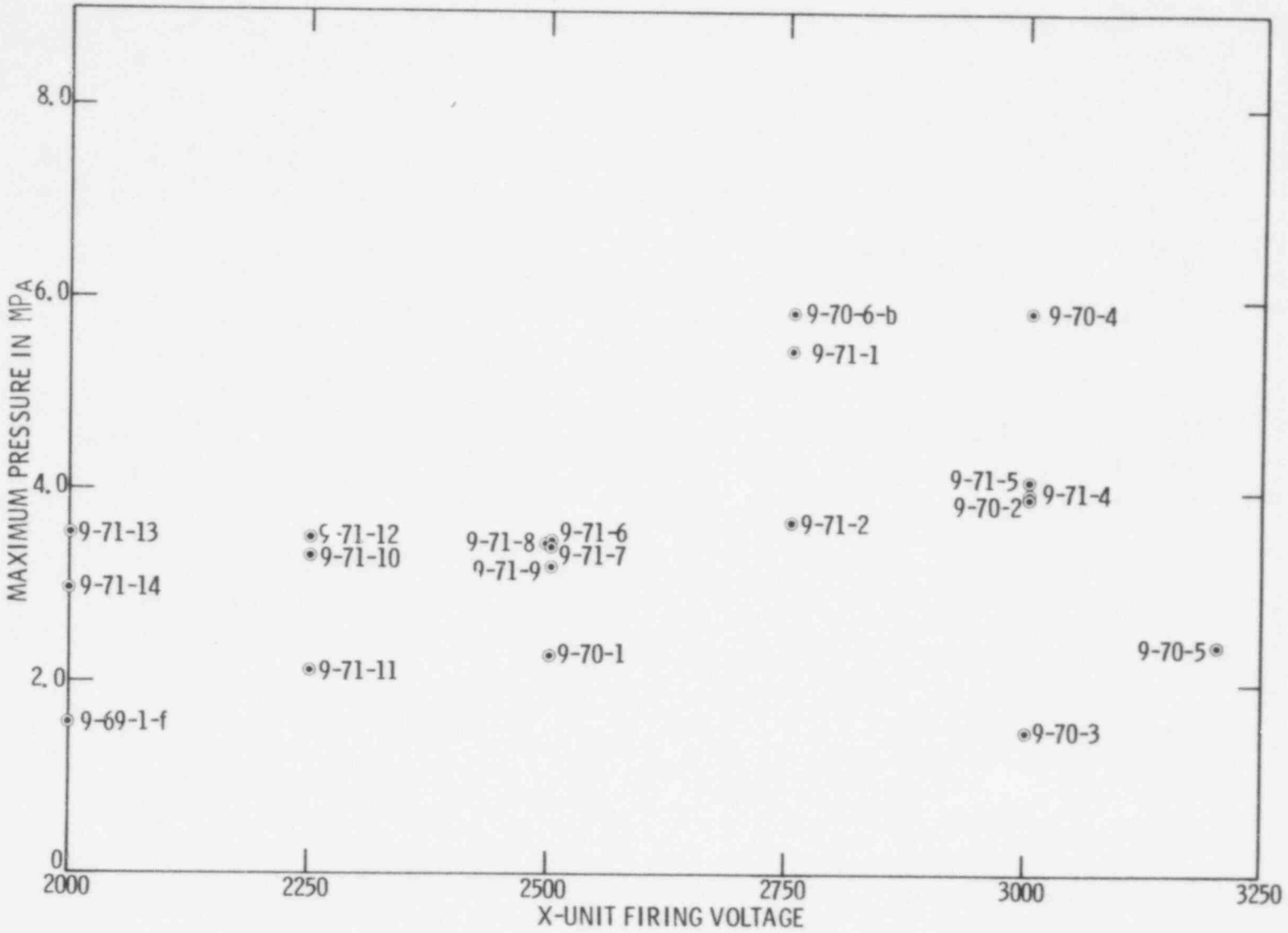

Figure 18. Peak pressures recorded in non-boiling water when various voltages were applied to the x-unit circuit which fires a submerged bridgewire. Lithium niobate transducer was at center of the apparatus, * 5 cm from bridgewire.

2.3.3 Mercury Motion Tests

A series of tests has been performed to determine whether the flooded melts which are exposed to detonator and bridgewire generated pulses are physically torn apart by the direct action of the pressure pulses or whether the fragmentation is a result of the melt-water interaction. A mockup vessel was made from the bottom portion of an aluminum pressure cooker with dimensions essentially identical to those of the interaction chamber. The top of the vessel was covered with a 1/2-inch thick transparent polymethyl-methacrylate slab, through which a bridgewire or detonator and three pressure transducers were mounted. An unused, spare copper hearth was positioned at the center of the mockup vessel and 35 g of instrument grade mercury was placed in the depression in the hearth to produce a globule with the same volume as a 20-g globule of molten stainless steel. The components were each placed to simulate their actual positions in the interaction chamber in a triggering experiment. After filling with water, the mockup vessel was placed on the work stand in the exact position that the interaction chamber normally occupies in order to permit three-pulse flash x-ray imaging as in the triggering experiments. The Hycam camera was mounted above the vessel and pointed downward through the transparent cover to record any motion.

Eleven experiments with mercury were performed, one with a submerged detonator and ten with submerged bridgewires. In the experiment with the detonator, the growth of a large bubble in the water around the detonator site was readily observed in the high speed film. The gas bubble actually extended past the center of the hearth at its maximum size. The flash x-ray images showed coarsely fragmented mercury shortly after the detonator was fired.

In the bridgewire experiments, much smaller bubbles which collapsed prior to reaching the hearth were formed in the water and only a gentle undulation of the mercury could normally be detected. In the one exceptional bridgewire experiment, what appeared to be the blowing out of a mercury bubble and a small amount of coarse fragmentation were observed. In that experiment there was a small bubble of air, less than one millimeter in diameter, inadvertently trapped at the mercury-water interface prior to the interaction. However, in another experiment in which a small bubble of air was deliberately introduced at the mercury-water interface, only mild undulation could be seen.

It is assumed that the action viewed in these experiments is very similiar to that which occurs in the actual test chamber. Thus, it has been concluded that the mechanical action of the nearby bridgewire discharge does not seriously disrupt the liquid metal on the hearth and that the direct action of the detonator produces essentially only coarse fragmentation.

2.3.4 Gas Analyses of Stainless Steel

Type 304 stainless steel obtained from two different lots of original metal was analyzed for nitrogen, oxygen and hydrogen content by standard Leco fusion and gas analysis techniques. Eight samples were analyzed: two controls which were taken from Lots 1 and 2 without melting, and six samples which had been melted in various atmospheres. Two of the melted samples had also been flooded with water. A summary of the experimental results is shown in Table VIII. For comparison, the gas analysis of a sample of high quality iron which was obtained from Sandia's ferrous metal melting laboratory is also shown in Table VIII.

The nitrogen content of these stainless steels is relatively high, consistent with the metallurgical practice of nitriting the metal to enhance hardness. The oxygen content is not unusual for ferrous metals. The hydrogen content is relatively low, but apparently increases upon melting in our apparatus.

2.3.5 Melting Studies of Corium-E Simulants

The term "Corium" has been coined to denote the material which could form in the event of a core melt accident in a typical light water reactor. Peehs[11] has tabulated the compositions for Corium-A and Corium-E, the core meltdown material to be expected early and late in the accident, respectively, in terms of weight percent of stainless steel structural metal, zircalloy cladding, and uranium dioxide fuel.

During this quarter, work has been done with two different Corium-E simulant materials of simplified four-component (U-Zr-Fe-O) composition. These simulants are expected to behave much as "real" Corium-E which will have at least seven components (U-Zr-Fe-Cr-Ni-Sn-O-?), neglecting fission products. The composition of these simulants is given in Table IX. Since one is prepared from mostly metallic components, it is called the "metallic" Corium-E simulant,

764 275

TABLE VIII.

Gas Analyses of Metals Used in this Work

Material	Expt. No.	Oxygen (ppm/wt)	Nitrogen (ppm/wt)	Hydrogen (ppm/wt)	Sample Preparation
Stainless Steel (Type 304)	Control Lot 1	71±5	241±5	2.32±24	Control, ½" rod, Lot #1, as received.
	9-71-18	232±0	248±1	9.3	Argon, bottom inlet, slow cooling, old power supply.
	9-72-1	169±5	236±4	8.1	Argon/water vapor, bottom inlet, slow cooling, old power supply.
	9-72-2	189±5	249±7	9.3	Argon, top inlet, slow cooling, old power supply.
	Control Lot 2	49±3	160±1	1.73±0.10	Control, ½" rod, Lot #2, as received.
	9-73-2	19±4	154±2	1.9	Argon, top inlet, slow cool, new power supply.
	9-73-1	28±2	180±1	2.1	Argon. top inlet, flooded, old power supply. (Notebook says from Lot #1)
	9-81-2	19±12	136±1	2.8	Argon, bottom inlet, flooded, new power supply.
Iron	9-90-1	180±33	14±1	4.22±0.25	

TABLE IX.

Summary of Corium-E Simulant Compositions
Used in this Work

"METALLIC" CORIUM-E*

Fe	55 w/o
U_3O_8	35 w/o
Zr	10 w/o

"OXIDIC" CORIUM-E*

Fe_2O_3	61 w/o
U_3O_8	28 w/o
ZrO_2	11 w/o

*Atom Ratios of Metals are Held Constant.

while the other, made up completely from oxides, is called the "oxidic" simulant. In both cases, the samples were prepared by cold pressing the appropriate powder mixtures.

The "metallic" Corium-E simulant was quite difficult to melt even with the new power supply. On partial melting, the material quickly separated into at least a two-phase mixture, one phase being metallic with a low emissivity and the other phase being non-metallic with a high emissivity.

The samples seemed to retain a non-metallic layer at the top which apparently volatized to form concave pits just below the electrodes. The original pellet shape was partially deformed but basically intact. Sessile drops were not achieved. After solidification, the samples were magnetic.

Photographs of one sample (9-74-3) are shown in Figure 19 both as cooled and after cross sectioning. This particular sample was prepared from two stacked pellets of pressed powders. A photograph of a more typical sample of "metallic" Corium-E simulant (9-74-2) prepared from a single pellet of pressed powders is shown in Figure 20-a. Figure 20-b is a photograph of that same sample after it was cut in half. The striations are sawing marks. Figure 20-c is a low magnification photograph of one of the sample halves which has been potted in an epoxy composition and polished in preparation for electron microprobe studies. Figure 20-d is a schematic of the polished piece used to indicate areas of importance in the following discussion.

Figure 20-e is a relatively high magnification (200X) optical photograph of area 2. As evident in Figure 20-e, there is an obvious change in porosity in that area with the low porosity portion being representative of area 1 and the high porosity portion being representative of area 5. Apparently, the low porosity material in area 1 is a well melted and mixed portion which flowed there from the original confines of the pellet. Note that the line denoted by 6 in Figure 20-d is the original (but tilted) pellet edge.

Figure 21 is a set of electron microprobe images taken in area 1 at a magnification of 500X. The upper photograph is from the scanning electron microscope mode while the lower photographs are for the same spot in the elemental scanning mode. As shown in Figure 21-a, there is no evidence of

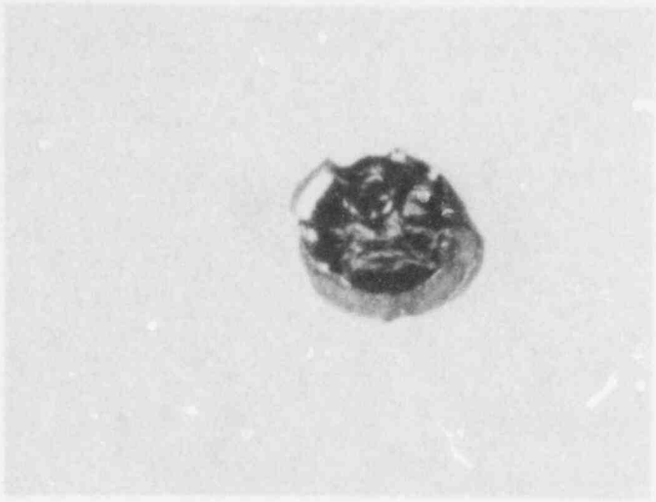

Original

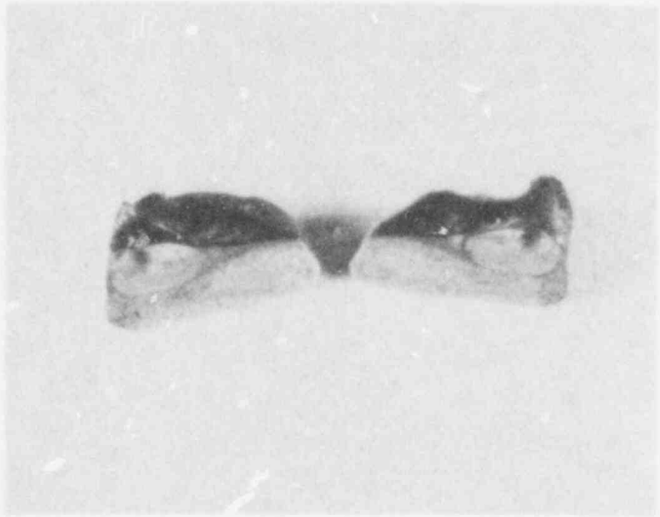

Cross Section

Arc-melted "metallic" Corium-E frozen in argon

(9-74-3)

Grid: 6.4 mm

Figure 19. Arc melted "metallic" Corium- E simulant prepared from two stacked pellets. In original above, the sample as frozen in argon, and cross section below, after cross sectioning.

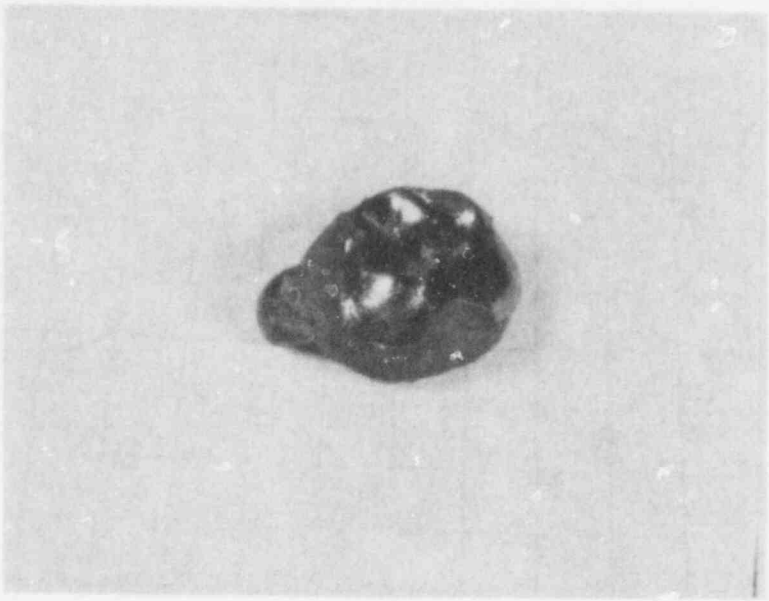

(a) As retrieved from arc melter. Grid = 6.4 mm.

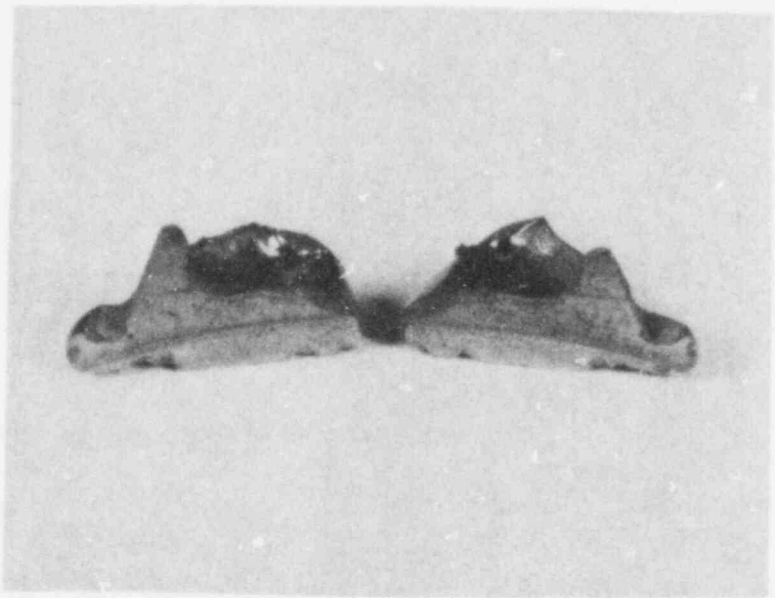

(b) Cross sectioned. (Horizontal band at center of the sample is due to saw). Grid = 6.4 mm.

Figure 20. Arc-melted "metallic" Corium-E simulant frozen in argon.

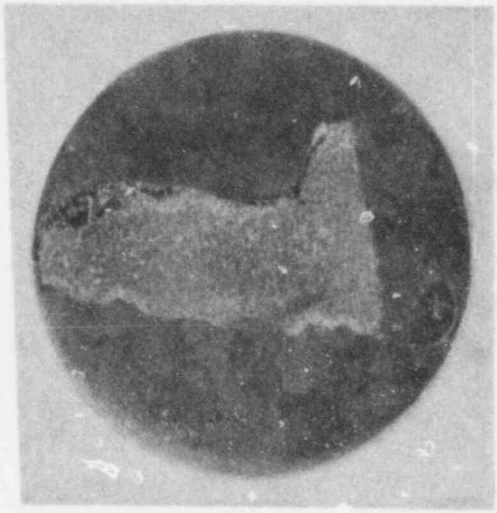

(c) Right hand portion of b polished for metallographic and electron microprobe examination.

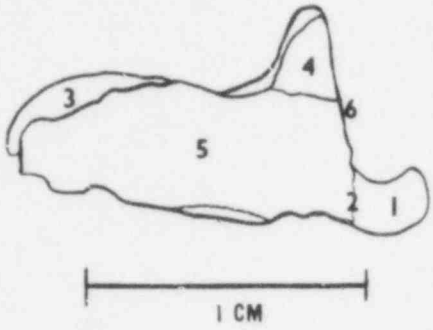

(d) Schematic of c:
Area 1 is highly reflective;
Area 2 is interfacial region;
Area 3 is slag;
Area 4 is porous with slag;
Area 5 is porous region;
Line 6 is original pellet edge.

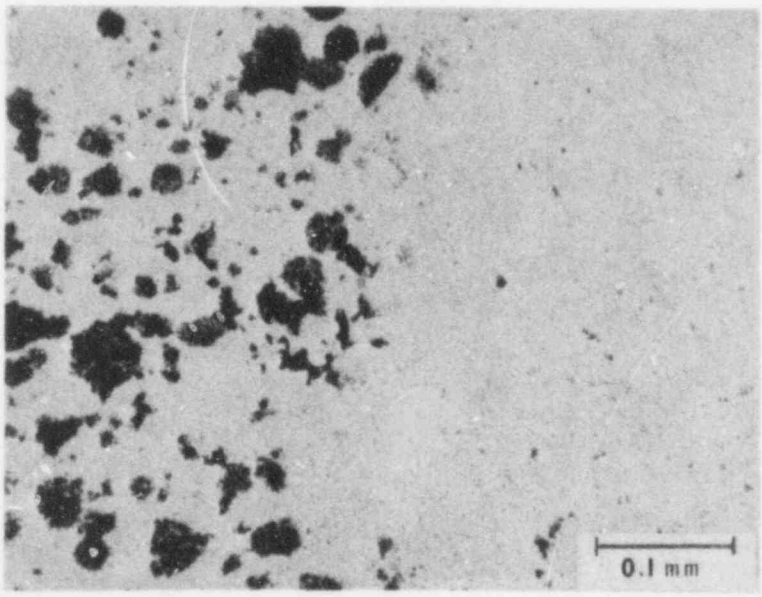

(e) Photomicrograph of interfacial Area 2.

Figure 20. (Cont'd.) Arc-melted "metallic" Corium-E simulant frozen in argon.

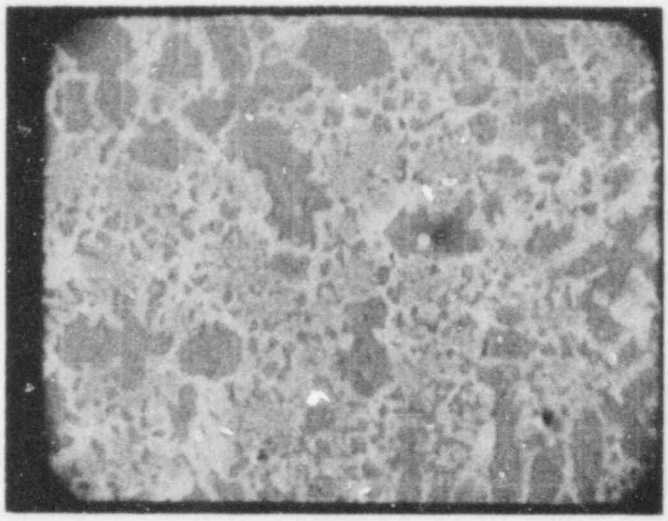

(a) Scanning Electron Micrograph

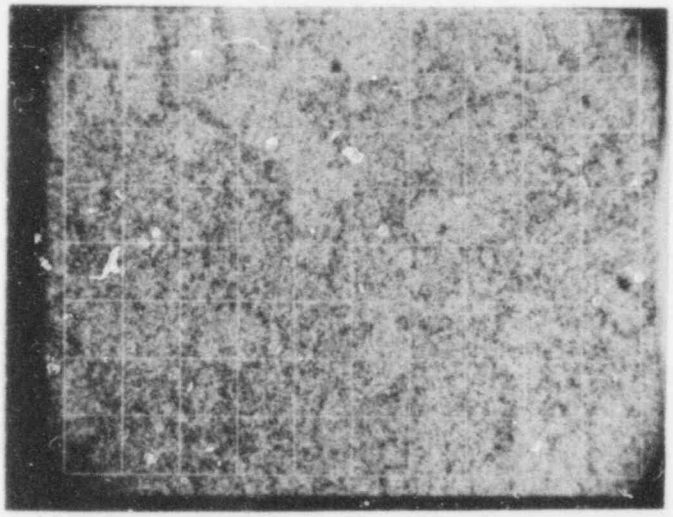

(b) Ps 16 Seconds

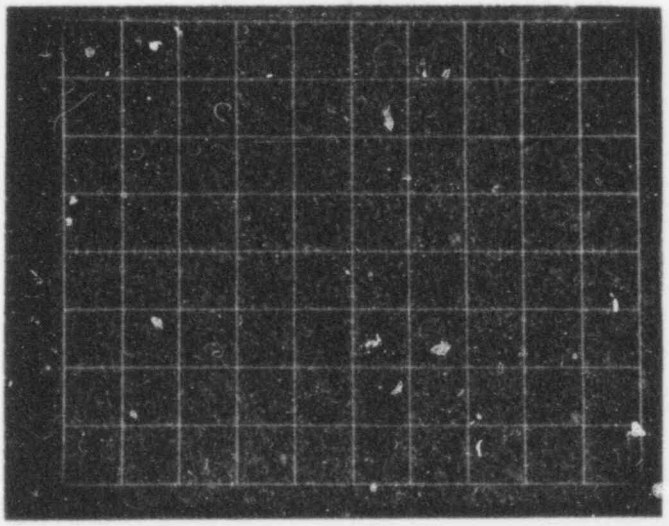

(c) 0 8 Minutes

Figure 21. Electron microprobe scans of Area 1 in Figure 20-d. One large grid division = 20 micrometers.

764 282

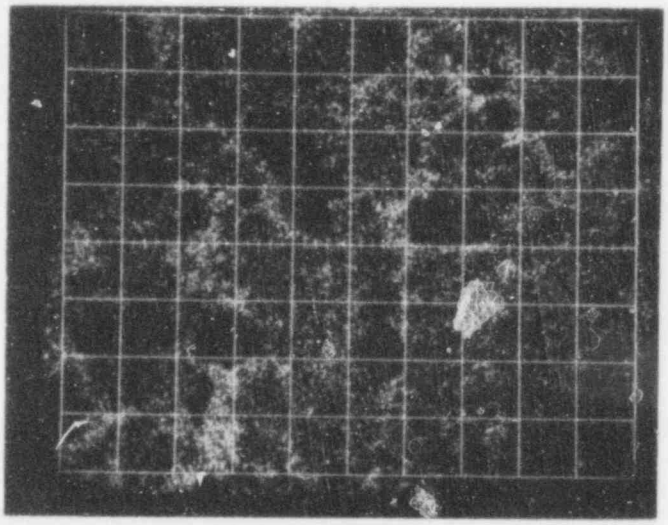

(d) U 3 Minutes

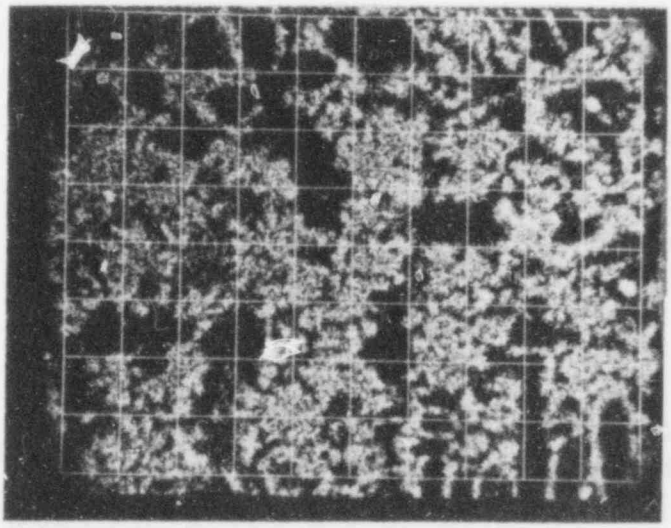

(e) Zr 3 Minutes

Figure 21. (Cont'd.) Electron microprobe scans of Area 1 in Figure 20-d. One large grid division = 20 micrometers.

significant porposity in area 1. The atomic scans in Figures 21-b, -c, -d, and -e indicate the iron is fairly homogeneously distributed throughout area 1 although there is some depletion of the iron in regions rich in U and Zr. The U and Zr seem to be present together in a we ing network as if they were combined in the same crystalline structure. The oxygen seems to be fairly homogeneously distributed in area 1 of the sample.

Perhaps not entirely obvious in the reproduced photograph in Figure 21-a, but certainly evident in the original scanning electron micrograph, is the fact that three distinctly different colorations are present. The webbing is composed of both a white portion and a light grey portion while the interstices in the webbing are filled with dark grey appearing material. This basic coloration scheme is true for all of the microprobe photographs to be discussed. In each case the white portion is rich in U and deficient in Fe and Zr. The light grey portion is rich in Zr, contains some U, but is deficient in Fe. The dark grey area is rich in Fe and deficient in both Zr and U.

Figure 22 is a set of microprobe images taken in the interface area 2 of the sample. When orienting these images with the schematic in Figure 20-d, one should mentally rotate these photographs ninety degrees counterclockwise. It is then obvious the dark spots in Figure 22-a represent the pores seen in the optical photograph in Figure 20-e. By comparison with Figure 21, it is also seen that the sample structure is more heterogeneous in the bulk of the sample than in area 1, the protuberance. The elemental microprobe scans further indicate that in area 2 the oxygen is predominately with the U, there has been little combination of Zr and U on the microscopic scale and even less combination of Fe and U. Other microprobe scans performed in area 5 indicate very similar structure to that seem in Figure 22.

Figure 23 is a set of microprobe images taken in area 3 of the sample. This material was referred to earlier as being non-metallic. It is also thought of as a slag. As seen in Figure 23, this area contains virtually no Fe and basically consists of a very homogeneous mixture of U, Zr, and O which is quite different from the structure of the bulk of the sample.

764 284

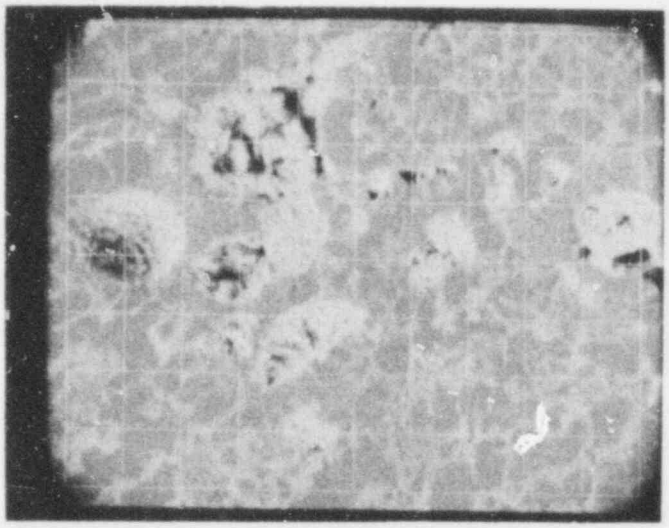

(a) Scanning Electron Micrograph

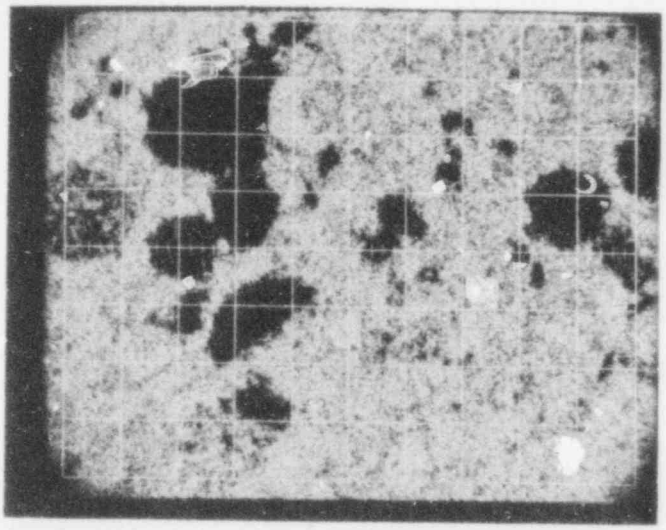

(b) Fe 16 Seconds

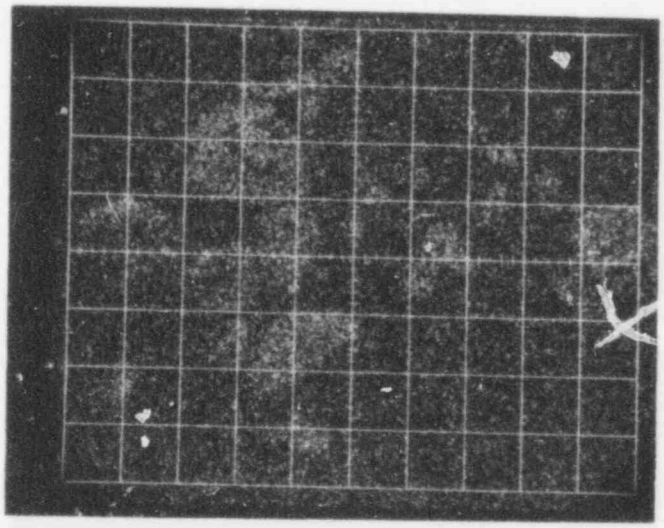

(c) O 8 Minutes

Figure 22. Electron microprobe scans of Area 2 in Figure 20-d.
One large grid division = 20 micrometers.

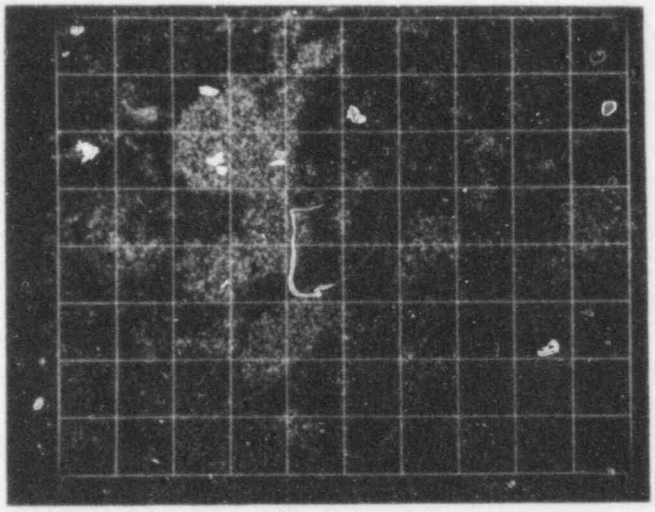

(d) U 3 Minutes

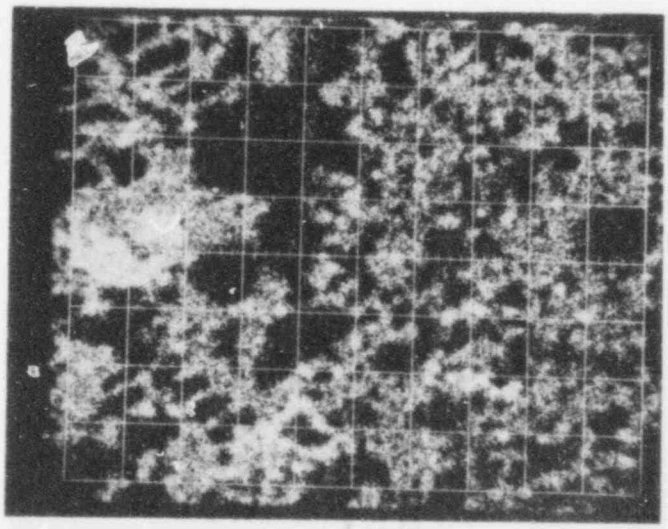

(e) Zr 3 Minutes

Figure 22. (Cont'd.) Electron microprobe scans of Area 2 in Figure 20-d. One large grid division = 20 micrometers. 764 286

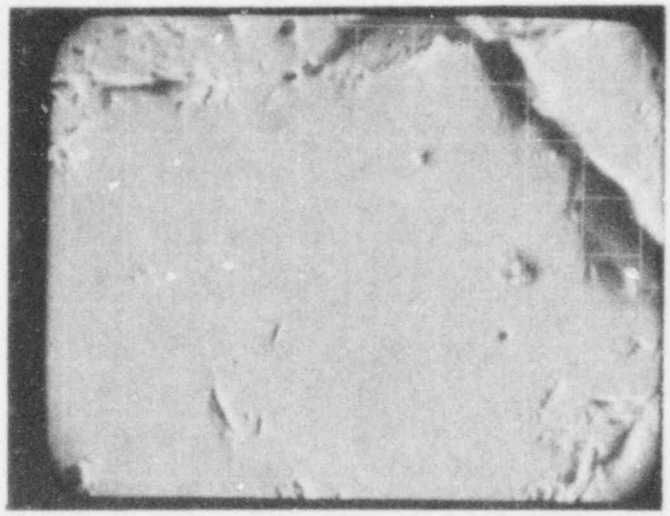

(a) Scanning Electron Micrograph

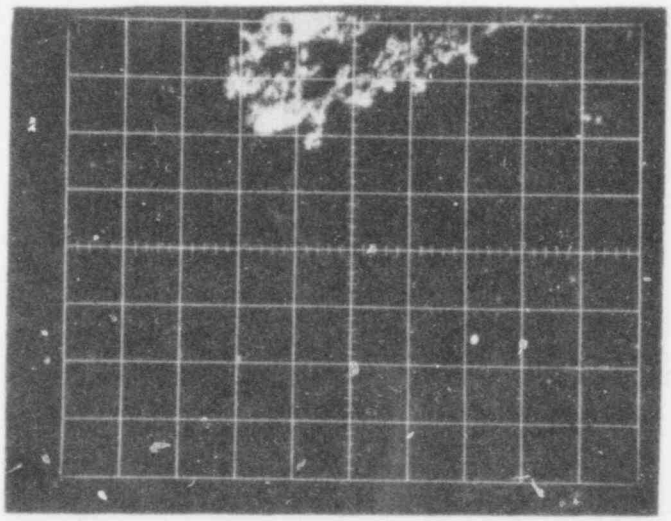

(b) Fe 1 Minute

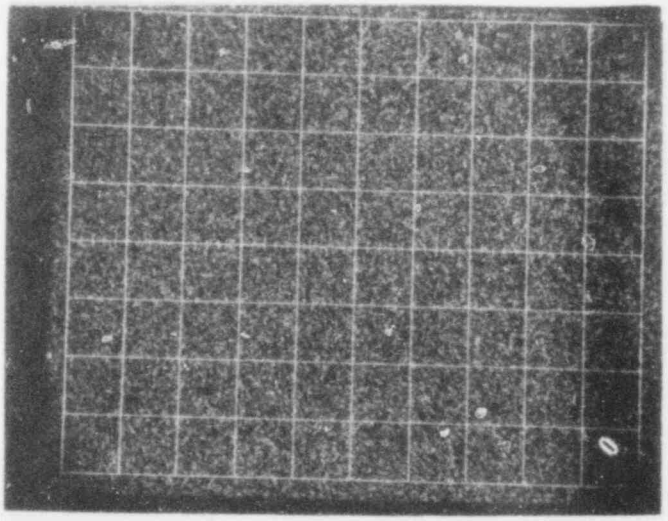

(c) O 8 Minutes

Figure 23. Electron microprobe scans of Area 3 in Figure 20-d.
One large grid division = 20 micrometers.

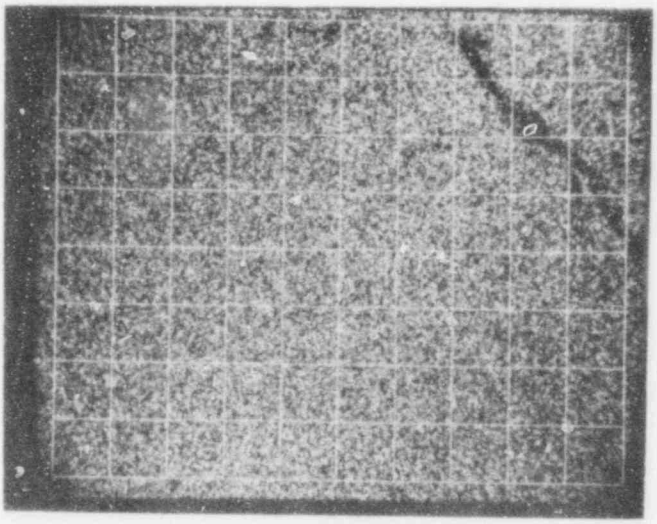

(d) U 1 Minute

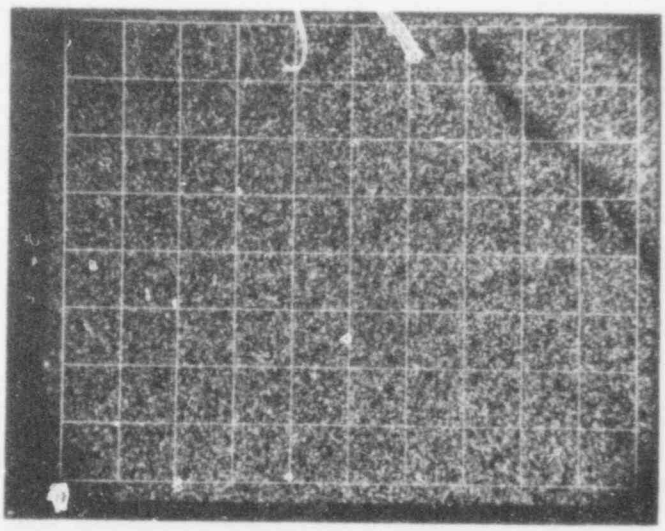

(e) Zr 1 Minute

Figure 23. (Cont'd.) Electron microprobe scans of Area 3 in Figure 20-d. One large grid division = 20 micrometers.

The melting situation was markedly different with the "oxidic" Corium-E simulant. In argon, the samples melted easily to what seemed visually to be a well-behaved, low viscosity, one-phase liquid at temperatures of 1875-2075 K (optical pyrometer results, assuming an emittance of 1.0 at 0.8 micrometers). Vaporization was not a serious problem. The material froze in argon to form a globule with a smooth black surface. The solidified sample was apparently highly stressed and easily cracked or shattered at room temperature. Figure 24-a is a photograph of such a globule of the "oxidic" material which had frozen in argon and cracked into four large pieces during the freezing process. It is seen to have a fairly large central void and several smaller cavities. The material is magnetic.

One piece of this frozen "oxidic" sample was polished and subjected to electron microprobe analysis. Figure 24-b is a low magnification photograph of the potted and polished piece. The round and oval appearing areas are small cavities which were filled with epoxy during potting.

Figure 25 is a set of microprobe images taken in the triangular area in the lower left corner of the piece shown in Figure 24-b. The scanning electron micrograph and elemental scans look similiar to those for the "metallic" material in Figure 21 but the O is not distributed as homogeneously. Also the O is found to be located primarily with the Fe instead of with the U as shown for the "metallic" simulant area shown in Figure 22. This behavior is not surprising since the starting powder for the "oxidic" material was Fe_2O_3 instead of Fe.

Figure 26 is a set of images taken in the dark upper right hand area of the piece of "oxidic" Corium-E. These images are very interesting because all of the constitutive elements appear to be fairly homogeneously distributed except in the two tree-like structures. These areas are almost totally devoid of U and Zr. Quantitative microprobes indicate the "trees" are Fe_3O_4 crystals. It is also interesting to note that little, if any, porosity is seen on the small scale even though large cavities are present in this area of the sample.

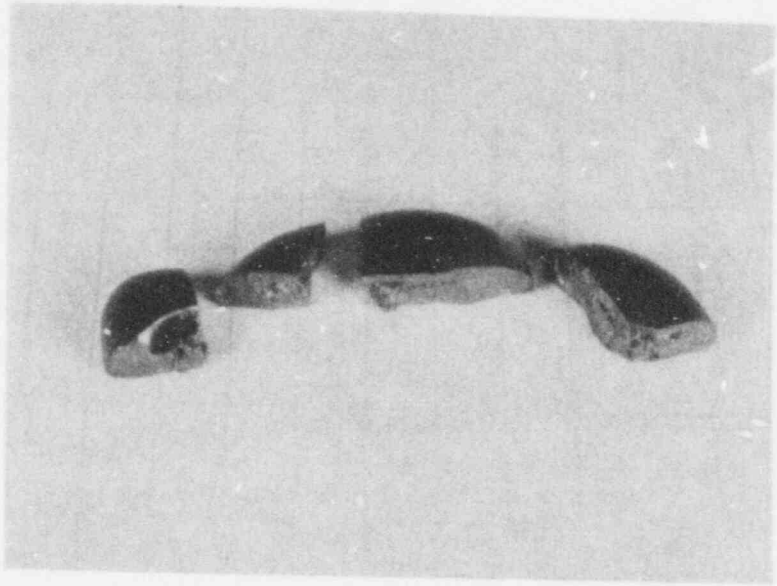

(a) As retrieved from arc melter. Grid = 6.4 mm.

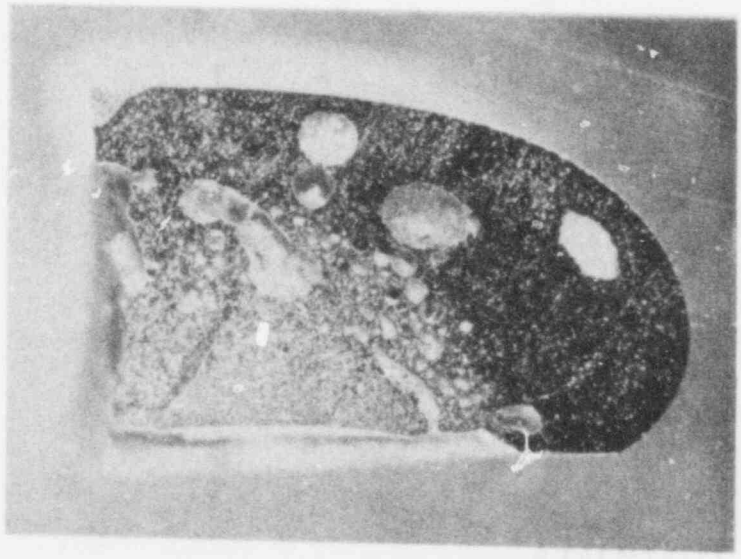

(b) Second chunk from left in a polished for metallographic and electron microprobe examination.

Figure 24. Arc-melted "oxidic" Corium-E simulant frozen in argon.

9-89-3

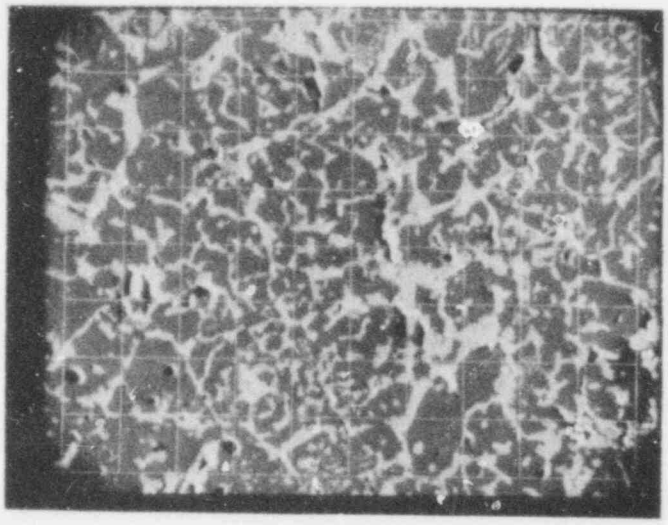

(a) Scanning Electron Micrograph

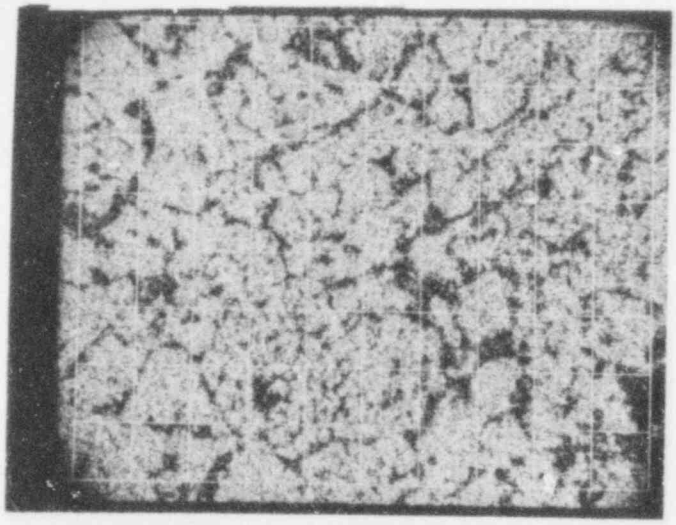

(b) Fe 16 Seconds

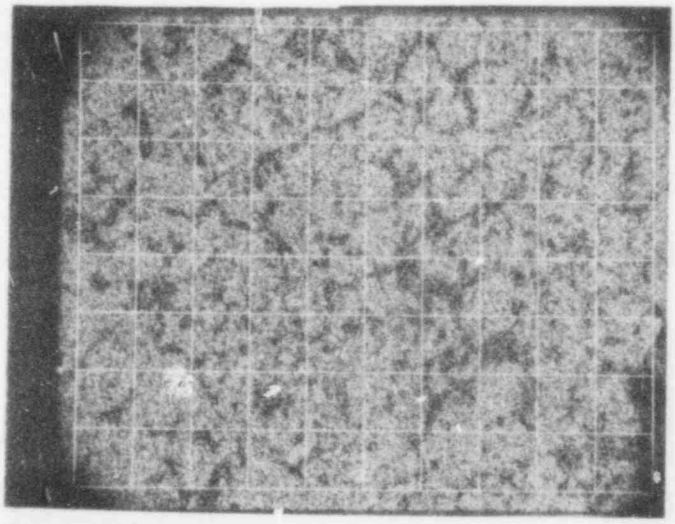

(c) O 30 Min

Figure 25. Electron microprobe scans of triangular area of [illegible] the sample shown in Figure 24-b. One large grid division = 20 micrometers.

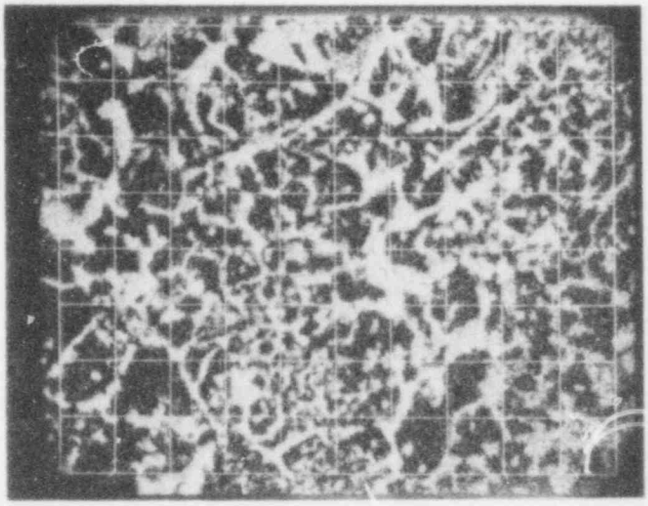

(d) U 6 Minutes

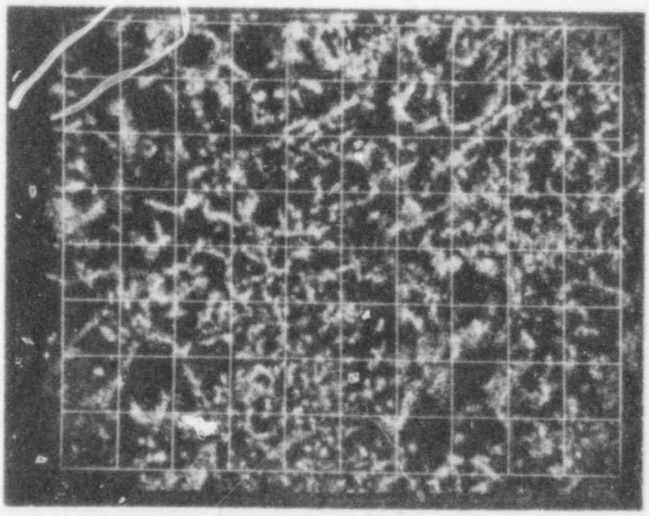

(e) Zr 6 Minutes

Figure 25. (Cont'd.) Electron microprobe scans of triangular area of the lower left corner of the sample shown in Figure 24-b. One large grid division = 20 micrometers.

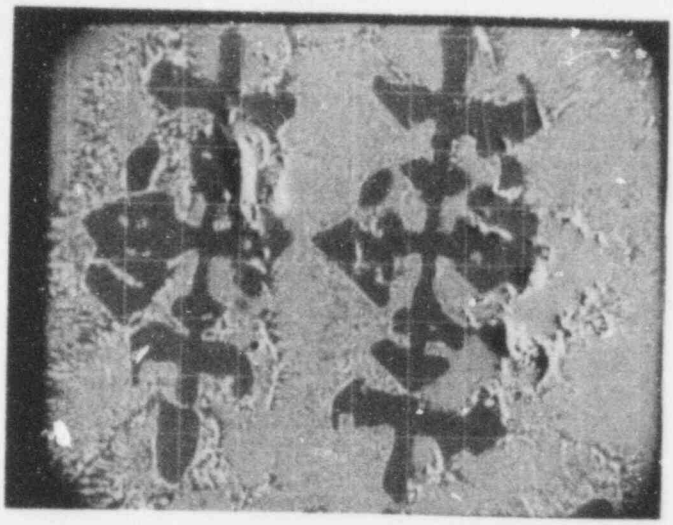

(a) Scanning Electron Micrograph

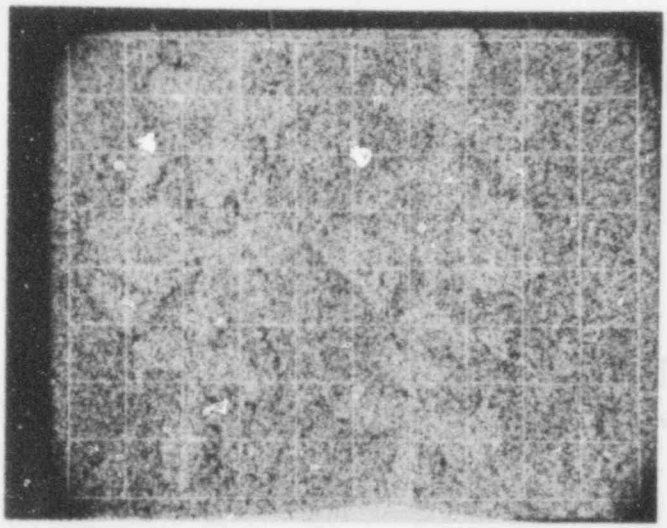

(b) Fe 16 Seconds

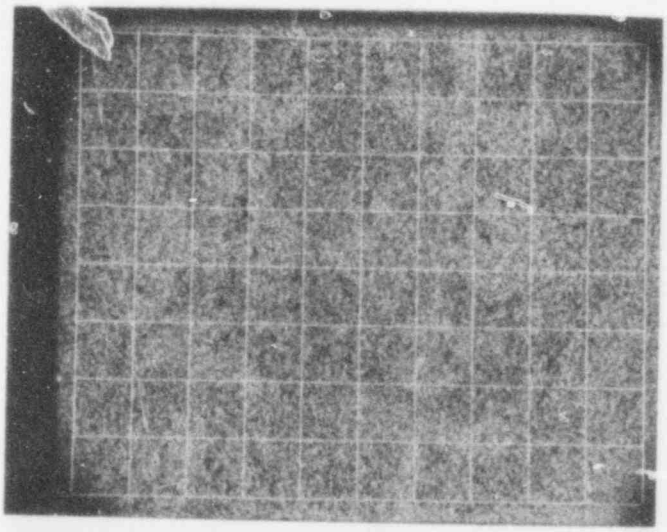

(c) O 30 Minutes

Figure 26. Electron microprobe scans of dark upper right-hand area of the sample shown in Figure 24-b. One large grid division = 20 micrometers.

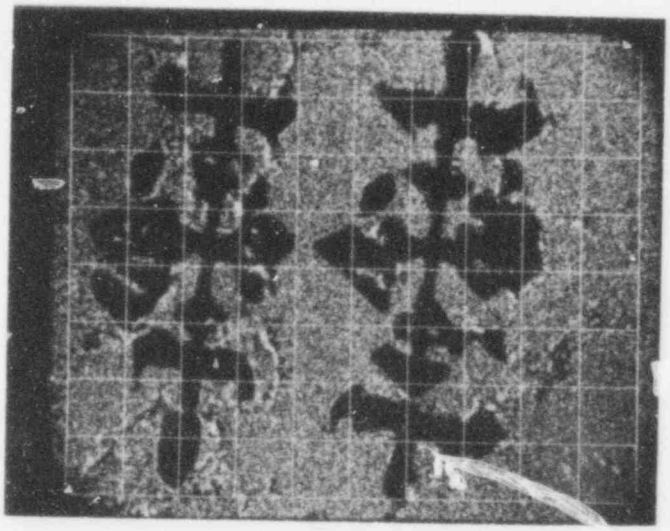

(d) U 6 Minutes

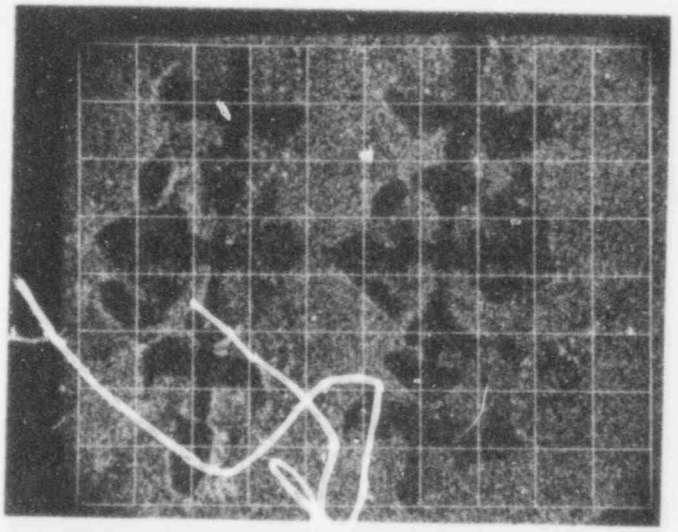

(e) Zr 6 Minutes

Figure 26. (Cont'd.) Electron microprobe scans of dark upper right hand area of the sample shown in Figure 24-b. One large grid division = 20 micrometers.

2.4 Results of Triggering Experiments

2.4.1 Summary

During this quarter, twelve samples of stainless steel and seven samples of "oxidic" Corium-E simulant were arc-melted with the new power supply and flooded with water. The results of these experiments are summarized in Table X, which is a continuation of Table XVIII in SAND76-0677[2] and Table I in SAND77-0214[9].

2.4.2 Stainless Steel Experiments

As shown in Table X, the twelve stainless steel experiments were comprised of eleven in which bridgewires were fired as the pressure transient generator and one in which a detonator was fired. The experiment with the detonator (9-75-1) went smoothly and all instrumentation operated properly. Considerable coarse fragmentation occurred in this experiment although, based on the experience with the mercury, some of the breakup may have been caused by the direct action of the detonator blown bubble. The flash x-ray image of the sample recorded 20 milliseconds after the detonator was fired is shown in Figure 27; a photograph of the residue is shown in Figure 28. A mild return pressure pulse with a peak magnitude of approximately 4 bars was recorded in the water 0.9 milliseconds after the detonator was fired.

The stainless steel triggering experiments performed with bridgewires were plagued by sleeve release malfunctioning due to the increased heating with the new power supply. Since the springs were actually within the arc melting chamber during the experiments, they were exposed to high heat fluxes and consequently often fatigued prior to the time at which sleeve rise was to occur. As discussed earlier, this problem has now been resolved.

There were, however, four successful experiments in which considerable fragmentation occurred (9-78-1, 9-78-2, 9-80-1 and 9-82-2). The first two were performed with argon-water vapor melting atmospheres and the latter two with nominally pure argon melting atmospheres. An example of the coarse fragmentation of the stainless steel samples seen in the bridgewire triggering experiments is shown in the photograph in Figure 29 (9-80-1) and in the flash x-ray images in Figure 30. These multiple flash images were taken at 2, 4, and 20 milliseconds

TABLE X.

Summary of Results of Triggering Experiments

Material	Expt. No.	Sample Weight (gm)	Water Temp. (°C)	Water Amount (cc)	Melt Atm.	Melt Temp. (°C)	Transient Generation	Delay Time (sec)	Flash X-Ray	High Speed Photo	Remarks
304SS, ½", Lot 2	9-75-1	19.9	17.8	1500	Ar	1728	DET	*1.00*	One-pulse	400 Ft.	Much fragmentation, stable grey colloid formed in water-possible 4 bar return pulse.
304SS, ½", Lot 2	9-76-1	20.2	23.9	1500	Ar	1515	BW	0.942	One-pulse	400 Ft.	No fragmentation.
304SS, ½", Lot 2	9-77-1	20.3	15.2	1500	Ar/H_2O	1585	BW	0.946	One-pulse	400 Ft.	No fragmentation.
304SS, ½", Lot 2	9-78-1	19.6	18.9	1500	Ar/H_2O	1661	BW	0.452	One-pulse	400 Ft.	Flash x-ray image shows inflated sac above sample. Some fragmentation.
304SS, ½", Lot 2	9-78-2	20.5	14.9	1500	Ar/H_2O	1566	BW	0.462	Two-pulse	400 Ft.	Flash x-ray images show some efflorescence. Wrinkled sheet of frozen metal.
304SS, ½", Lot 2	9-79-1	20.0	17.8	1500	Ar	1547	BW	0.50*	Three-pulse	No image	Solidified globule. Flooding malfunction; sleeve failed to rise.
304SS, ½", Lot 2	9-80-1	20.3	14.6	1500	Ar	1566	BW	0.468	Three-pulse	400 Ft.	Flash x-ray images show efflorescence, some fragmentation.
304SS ½", Lot 2	9-81-1	20.3	12.5	1500	Ar	1553	BW	0.25*	Three-pulse	No image	Solidified globule. Flooding malfunction; sleeve failed to rise.
304SS ½", Lot 2	9-81-2	20.4	18.9	1500	Ar	1559	BW	0.25*	Three-pulse	No image	Solidified globule. Flooding malfunction; sleeve failed to rise.
304SS, ½", Lot 2	9-82-1	20.5	17.7	1500	Ar	1595	BW in cover gas	0.25*	Three-pulse	None	Solidified globule.
304SS, ½", Lot 2	9-82-2	20.1	15.4	1500	Ar	Strange	BW	0.183	Three-pulse	400 Ft.	Flash x-ray images show efflorescences fragmentation.
304SS, ½", Lot 2	9-83-1	20.6	20.0	1500	Ar	1580	BW	0.043	Three-pulse	400 Ft.	Solidified globule. Pressure transient applied before flooding was completed.
"Oxidic" Corium-E	9-91-1	15.3	19.8	1500	Ar	Window Fogged	BW	0.441	Three-pulse	400 Ft.	Complete fragmentation, stable colloid in water. No detector for return pulses.
"Oxidic" Corium-E	9-92-1	13.8	36.8	1500	Ar	1732a	None	---	Three-pulse	400 Ft.	Solidified globule with some internal bubbles. (Control Experiment)
"Oxidic" Corium-E	9-92-2	15.6	25.8	1500	Ar	Window Fogged	BW	0.429	Three-pulse	400 Ft.	Complete fragmentation, 7 bar return pulse, 2.5 msec after BW.
"Oxidic" Corium-E	9-93-1	15.5	32.1	1500	Ar	Very Low	BW	0.50*	Three-pulse	400 Ft.	Solidified globule; probably cold when flooded, due to malfunction.
"Oxidic" Corium-E	9-94-1	14.5	20.5	1500	Ar	1730a	None	---	Three-pulse	400 Ft.	Solidified globule, (Control Experiment)
"Oxidic" Corium-E	9-95-1	15.4	20.6	1500	Ar	1782a	BW	0.418	Three-pulse	400 Ft.	Complete fragmentation, 2.7 bar return pulse, 1.0 msec after BW.
"Oxidic" Corium-E	9-96-1	15.7	28.1	1500	Ar	Window Fogged	BW	0.396	Three-pulse	400 Ft.	Complete fragmentation, 7 bar return pulse, 3.5 msec after BW.

* Taken from apparatus settings; not measured on films.

a Calculated on the assumption that the emittance of the "oxidic" Corium-E melt is 1.0, and that of molten stainless steel is 0.3 at 0.8 micrometer wavelength.

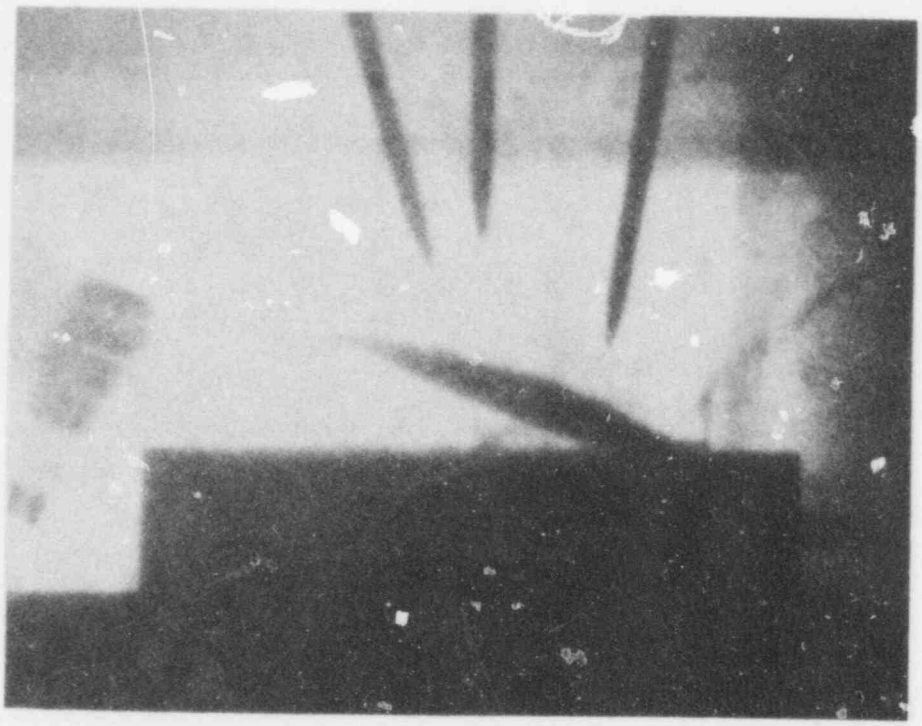

Figure 27. Flash x-ray image of molten stainless steel sample which has been flooded with water and subjected to a detonator pulse ≈ 1 second afterward. Flash x-ray image was recorded 20 milliseconds after the detonator fired. Rectangular image below the sample is the copper hearth, which is 5.8 cm across. Image at left is detonator. Three pointed rods above are electrodes.

Figure 28. Debris produced when molten stainless steel was flooded with water and subjected to a detonator pulse ≈ 1 second later. Grid = 6.4 mm.

9-75-1

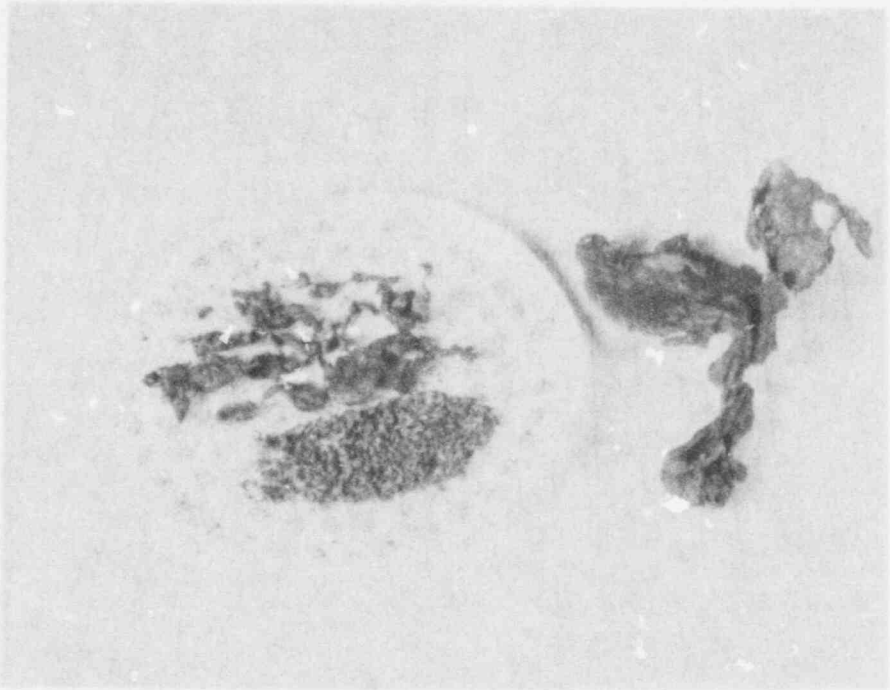

Figure 29. Debris retrieved from an experiment in which molten stainless steel was flooded with water and subjected to a pressure transient generated by an exploding wire. The pressure transient was applied 0.47 seconds after flooding was initiated. Grid = 6.4 mm

9-80-1

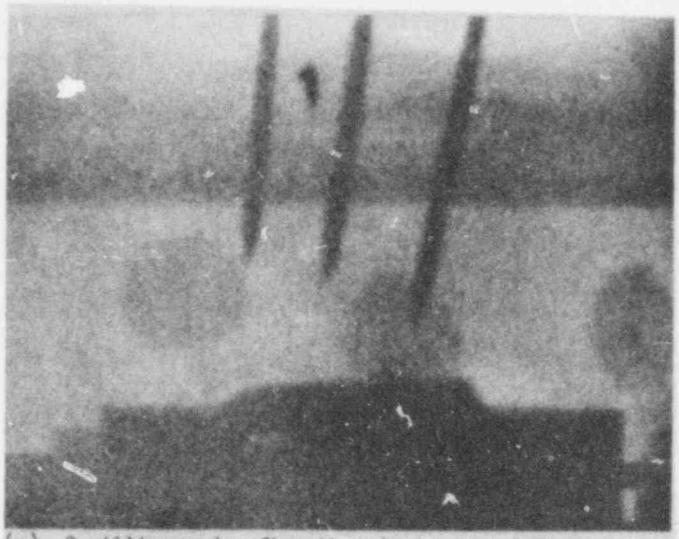

(a) 2 milliseconds after the wire was exploded.

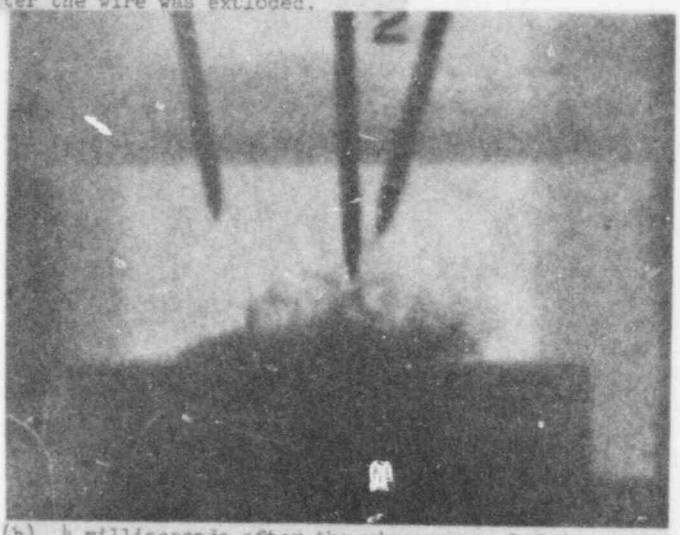

(b) 4 milliseconds after the wire was exploded.

(c) 20 milliseconds after the wire was exploded.

Figure 30. Flash x-ray images of molten stainless steel sample which had been flooded with water and subjected to a pressure transient from an exploding wire 0.47 seconds afterward. Images recorded shown above. Rectangular images at the bottom of the exposures are of the copper hearth, which is 5.8 cm across. Pointed rods are the arc electrodes.

9-80-1

764 300

after bridgewire firing. The fragmentation of stainless steel occurred only in the presence of the pressure transient applied through the water; without it the sample would be neither deformed nor fragmented. There was no fragmentation when the bridgewire was fired in the cover gas above the water (9-82-1). In none of the bridgewire triggering experiments with stainless steel was there any detectable return pressurization following the fragmentation of the sample.

2.4.3 Triggering Experiments with Corium-E Simulants

Because of the difficulty of obtaining homogeneous, fluid melts, no flooding experiments were attempted with the "metallic" Corium-E simulant this quarter. Seven flooding experiments with "oxidic" Corium-E simulant were performed. As control experiments, two samples which weighed approximately 15 g each (9-92-1 and 9-94-1) were melted and flooded with cold water without applying a pressure pulse. These samples were retrieved as smooth globules, not unlike the one obtained from slow freezing in argon. There was evidence of void formation within the sample for those flooded as well as for the one frozen in argon. Figure 31 contains two photographs of pieces of sample 9-92-1 which was found to be cracked after the experiment, probably from thermal stress. Figure 31a is a photograph of approximately half the sample which clearly shows a large central cavity. Figure 31b shows at a higher magnification some smaller bubble-like voids found primarily on the underside of the "roof" of the large cavity.

A series of five experiments was performed where samples of the "oxidic" Corium simulant approximately 15 g in weight were flooded with cold water and exposed to pressure transients produced by firing bridgewires at 3 kV beneath the water ≈ 0.4 seconds after sleeve release (9-91-1, 9-92-2, 9-93-1, 9-95-1, 9-96-1). In four of the five experiments, extensive fragmentation occurred, there was a distinct "thud" audible during the interaction, and a heavy concentration of black material remained suspended in the water after the experiment. In the fifth experiment (9-93-1) there was hardly any interaction. After examination of the pyrometer trace and viewing the film, it was concluded that the arcs had extinguished prematurely, allowing the sample to freeze before flooding.

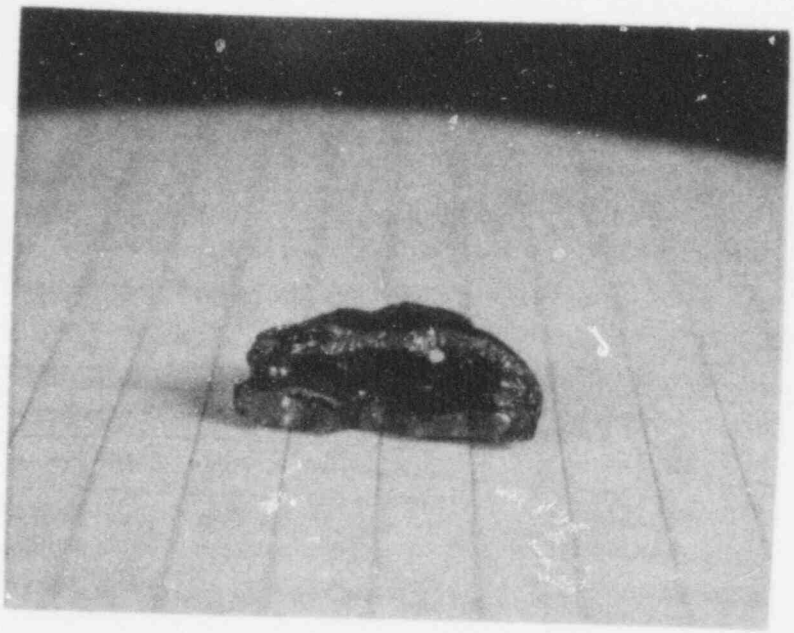

(a) Sample roughly in cross-section, showing large internal cavity and hole to outside at the rear. Grid = 6.4 mm.

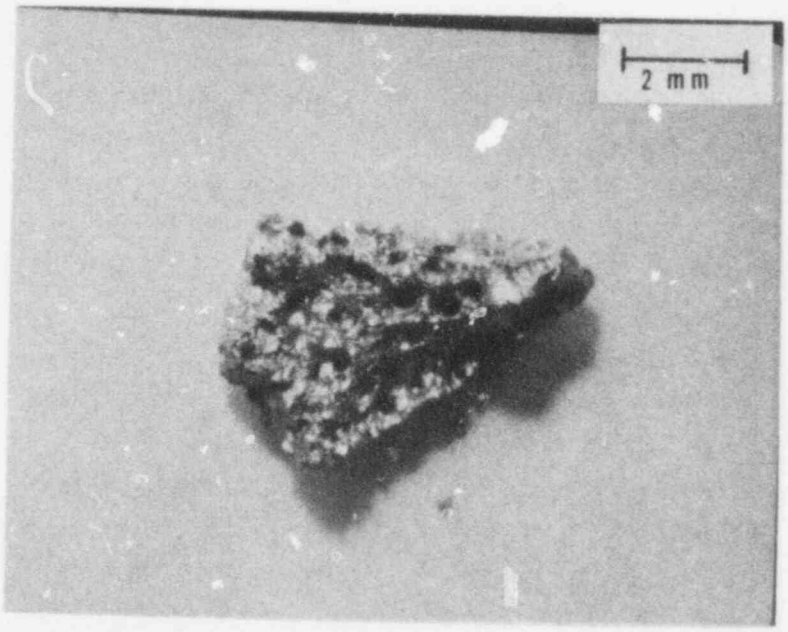

(b) Piece of the underside of the "roof" of the sample, showing bubble-like voids.

Figure 31. Sample of "oxidic" Corium-E simulant which, while molten, had been flooded with water. No pressure transient was applied.

9-92-1

For experiments 9-92-2, 9-95-1, and 9-96-1, transducer records indicated pulses of 7, 2.7, and 7 bars peak pressure returned after delay times of approximately 2.5, 1.0, and 3.5 milliseconds, respectively, from bridgewire firing. In experiment 9-91-1 there was no detector for return pulses operating but the high-speed movie indicated an explosion at a delay time of 4 milliseconds. Figure 32 is a reproduction of a dual oscilloscope trace from experiment 9-96-1. The top trace shows the pulse seen by a transducer in the water near the chamber wall. As mentioned, the peak magnitude corresponds to a pressure of approximately 7 bars at 3.5 milliseconds after bridgewire firing. The risetime is on the order of 100 microseconds and the duration of the positive portion of the pulse is approximately 1 millisecond. A broad, small magnitude tensile pulse is seen to follow the compressive pulse. The bottom trace is from a transducer in the cover gas. The scope sensitivity is a factor of four larger for that trace and a downward deflection indicates a pressure increase. A broad compressive pulse is seen which is only about a quarter of an atmosphere in magnitude. This compressive pulse is also followed by a broad tensile pulse of low magnitude.

In Figure 33 the debris which resulted from experiment 9-95-1 is shown. The largest particles are few in number and no more than a millimeter in diameter. The smallest particles, which are seen covering the filter paper, have diameters of a few tens of microns at most. Particle size analysis of the debris is underway. Figure 34 shows reproductions of the flash x-ray images taken during the generation of the debris. The images were recorded 2, 3.5, and 5 milliseconds after the application of the pressure transient to the water. The pointed rods are the arc electrodes. The discs in the background are the pressure transducers. The interesting streamer-like nature of the sample images should be noted. It should also be noted that all three images were recorded after the return pressure peak produced by the interaction had occurred.

2.4.4 Discussion and Analysis of Triggering Experiments

The stainless steel triggering experiments performed this quarter using the new current controlled power supply yielded somewhat different results than those stainless steel experiments performed with the old, lower power, potential controlled power supply used previously. The latest experiments using bridgewires for pressure

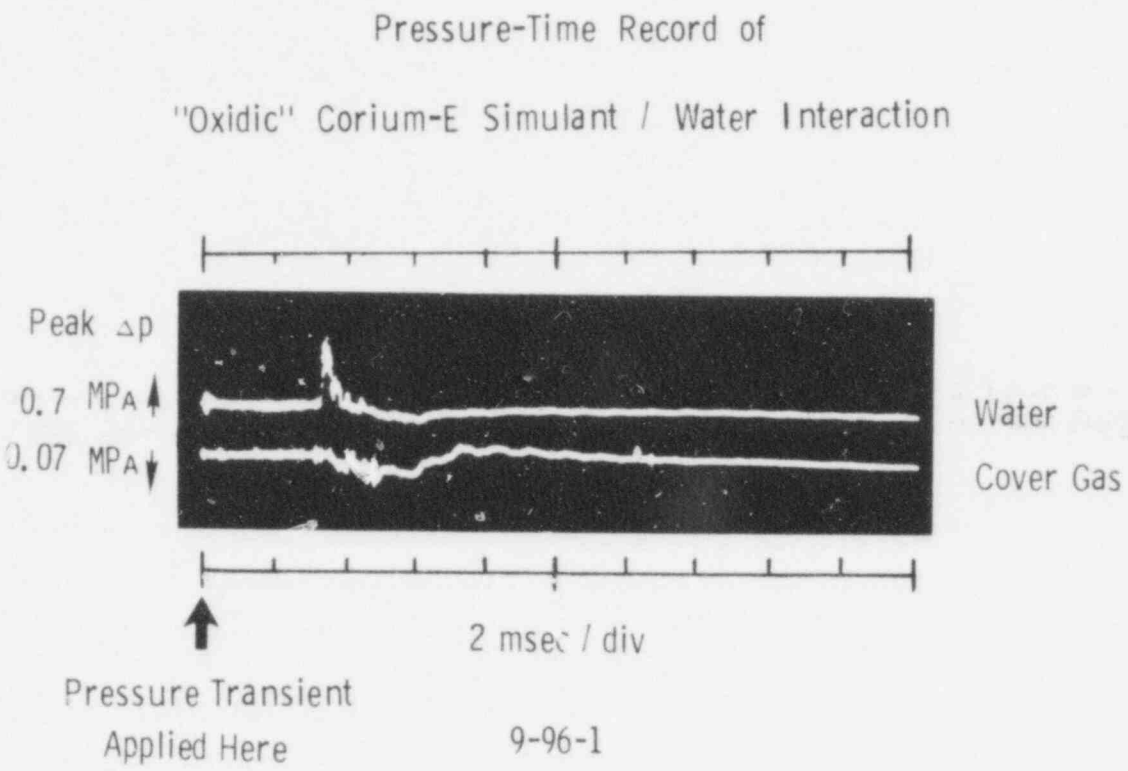

Figure 32. Pressure-time history of an experiment in which a molten sample of "oxidic" Corium-E simulant was flooded with water and subjected to a pressure transient generated by an exploding wire. The pressure transient was applied 0.40 seconds after flooding was initiated. Upper trace was recorded in the water; lower trace in the cover gas. Polarity is inverted in lower trace.

9-96-1

764 30-

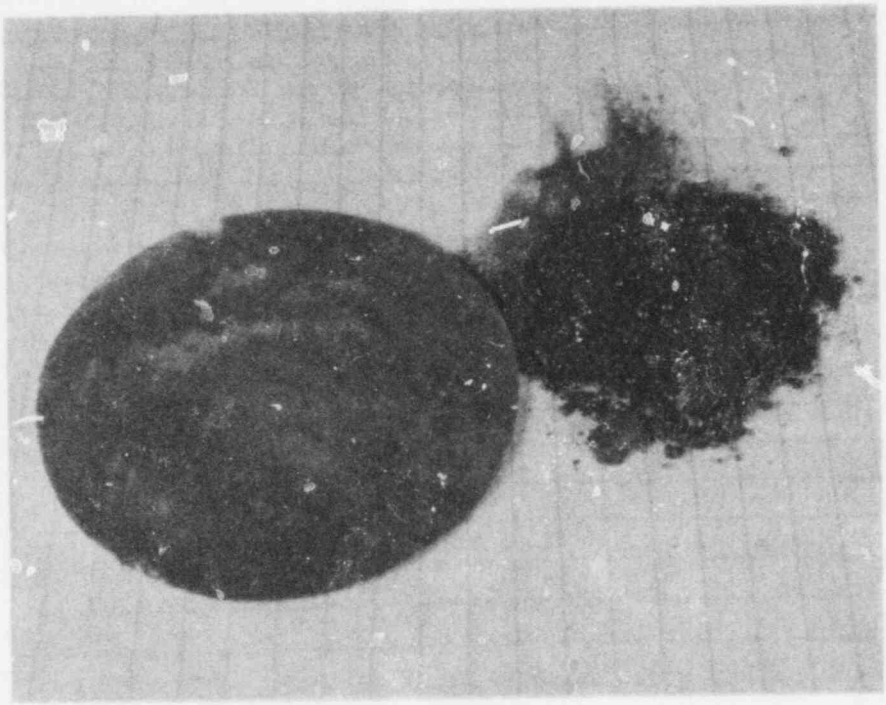

Figure 33. Debris retrieved from an experiment in which a molten sample of "oxidic" Corium-E simulant was flooded with water and subjected to a pressure transient generated by an exploding wire. The pressure transient was applied 0.42 seconds after flooding was iniated. Considerable fine material remains on the filter paper at the left. Grid = 6.4 mm.

9-95-1

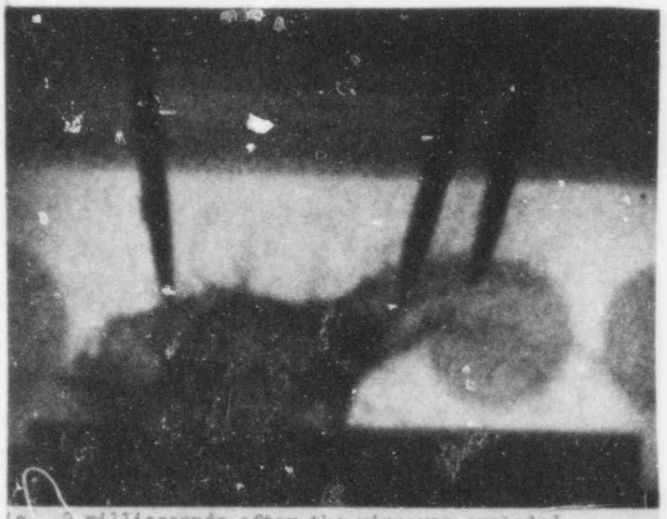

(a) 2 milliseconds after the wire was exploded.

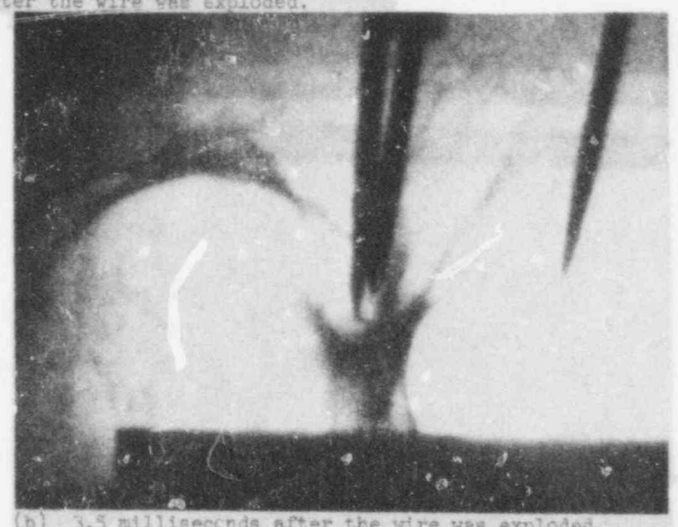

(b) 3.5 milliseconds after the wire was exploded.

(c) 5 milliseconds after the wire was exploded.

Figure 34. Flash x-ray images of molten "oxidic" Corium-E simulant which had been flooded with water and subjected to a pressure transient from an exploding wire 0.42 seconds afterward. Images recorded shown above. Rectangular image at base of (a) is the copper hearth, which is 5.8 cm across. Pointed rods are the arc electrodes.

transient generation exhibited considerably more fragmentation than the earlier bridgewire experiments with the old power supply.[2] In fact, the amount of stainless steel fragmentation observed in the latest bridgewire experiments is comparable to that obtained in the mini-detonator triggering experiments with the old power supply.[9] The single experiment performed with the new power supply using a mini-detonator as the pressure transient generator was noted earlier (in Section 2.4.2) to have generated a return pressure pulse approximately 4 bars in magnitude. The debris from that experiment, however, was qualitatively about the same as that obtained in the bridgewire triggering experiments which did not yield interaction generated pressure pulses.

A possible explanation for the increased fragmentation observed after changing the arc melter power supply is based on the pressure transient initiated gas release hypothesis for fragmentation which was briefly discussed in the July-September, 1976 quarterly report.[9] In that hypothesis, one source of releasable gas is the gases which might already be present in the original sample in a supersaturated state. If present, these gases will continually diffuse out of the sample, but the diffusion rate is extremely low and essentially zero at ambient room temperature. As the sample is heated, the diffusion rate increases considerably but the degree of supersaturation decreases as the temperature rises also. A shorter melting time allows less gas to diffuse out, consequently, with the new power supply and its associated shorter melting times, more gas is available to fragment the sample.

The series of triggering experiments performed this quarter with the "oxidic" Corium-E simulant has provided very interesting results. As reported in Section 2.4.3, those "oxidic" samples frozen in argon or flooded with water but not subjected to applied transients exhibited smooth outer surfaces (sometimes cracked) and contained large interior cavities with fairly porous roofs. The cavities in the flooded samples seemed to account for 30 to 40 percent of the total sample volume but only 10 to 20 percent of the volume for the sample frozen in argon.

There are at least two possible explanations for the formation of these large cavities. One is that the cavities are simply very large shrink cavities caused by a huge volume change at the freezing temperature. The cavities in the flooded samples, at least, seem to be far too large for that as a total explanation.

The possibility of spontaneous nucleation of a gas inside the sample upon cooling which inflates the sample and assists the shrink cavity formation is perhaps a more likely explanation. The porosity of the cavity roof would tend to support this argument since it is likely the roof was originally near a liquid-solid interface and the gas nucleation would be most likely to occur at such an interface. The gas release aspects would also account for the larger cavities in the flooded samples compared to the sample frozen in argon since more gas would presumably be released in the sample which has been cooled more rapidly.

The behavior of the "oxidic" Corium-E simulant samples flooded with water and subjected to bridgewire-generated pressure transients was quite different from the behavior of those which had been flooded without the pressure transients. As previously mentioned, explosive pressure pulses generated by the interaction (magnitudes of several bars with risetimes of less than a millisecond) were recorded at delay times of up to 3.5 milliseconds after the bridgewires fired. The high-speed motion pictures indicate a two-step interaction and confirm the delay times measured by the transducers. The films suggest a coarse fragmentation and mixing event roughly coincident with the applied pulse followed by the pressure producing explosion after a delay. The flash x-ray images show some fragmentation prior to the explosion but basically the sample appears to be intact and simply "fuzzy" on top until the explosion. Even after the explosion the sample fragments do not become randomly dispersed in the water but seem to form streamers or streaks which exist for at least several milliseconds.

The debris from these experiments has not yet been studied extensively, but it certainly contains many spherical particles which would suggest fragmentation of the sample while it was molten. There seem to be few broken shells to suggest that the spheres are hollow. Only a few large pieces remain afterward, indicating that the fragmentation in the triggered "oxidic" Corium-E simulant experiments is essentially total, unlike the stainless steel experiments where a solid bottom "plate" usually remained as well as possible pieces of a covering shell. However, since the "oxidic" material is extremely brittle, a bottom "plate" or a thin frozen layer could probably have been fragmented by the explosion. Few jagged fragments of significant size are seen, though. It is also possible that less of the "oxidic" material could have frozen prior to the interaction because of higher supercooling, earlier applied transients, or lower thermal conductivity effects.

Interpretation of the observed explosions is not at all complete at this time. As in the stainless steel experiments, a film boiling situation exists upon flooding which prevails until the sample is frozen unless a pressure transient is applied. When a transient is applied, the initial coarse fragmentation is not unlike that seen for the stainless steel. The same kind of impulse initiated gas release mechanism could account for the observed behavior except, for the "oxidic" Corium-E simulant, the possible gas sources would include superstoichiometric oxygen.

The explosive event which produces the return pressure pulse is not understood at this time. It could be caused by further gas release fragmentation triggered by some naturally occurring pulse or could have a totally different explanation such as superheating of the cold liquid during the delay period. Further investigation is required to determine the cause of the explosion.

2.5 Molten-Core/Water Contact Analysis

There are two new tasks in the fiscal year 1977 steam explosion phenomena program in addition to the continued triggering studies task. One of the new tasks is to evaluate the range of realistic conditions of contact between molten core components and water in hypothetical light water reactor fuel melt accidents. This task does not directly involve the mechanics of vapor explosions, but rather considers the availability of water in the lower head of the reactor vessel as a function of time and the rate at which molten core materials drop into the lower head.

The contact analysis task will basically consist of application and extension of the work performed in Appendix VIII of the Reactor Safety Study[12] on the thermal hydraulics of the core melting sequence. The tool used in that work was the BOIL code, developed by personnel of the Battelle Columbus Laboratory. Consequently, the first step in the contact analysis was to import BOIL from Battle. During the checkout of the code at Sandia, several programming errors were discovered. Those errors were discussed with Roger Wooten of Battelle and correction of them resulted in the BOILl code.[13] The errors were apparently not present when the Reactor Safety Study was performed but, in fact, were generated during a code rewrite before releasing it to the Argonne code center.

The basic models employed in the BOIL1 code were also checked this quarter for suitability and applicability to the problems of interest. The models were all found to be adequate for the initial calculations but not necessarily suitable for advanced studies. Final determination of the suitability of these simple models will be reserved until the initial calculations are performed.

2.6 Steam Explosion Scaling Studies

The second new task in the fiscal year 1977 steam explosion phenomena program is to plan an experimental and analytical program to investigate the effects of size scaling on the interaction of molten core materials and water. No reportable work was performed this quarter on that task.

REFERENCES

1. "Light Water Reactor Safety Research Program Quarterly Report, January-March 1976," SAND76-0369, Nuclear Fuel Cycle Safety Research Department, Sandia Laboratories, Albuquerque, NM, September 19, 1976.

2. "Light Water Reactor Safety Research Program Quarterly Report, April-June 1975," SAND76-0677, Nuclear Fuel Cycle Safety Research Department, Sandia Laboratories, Albuquerque, NM, February 1977.

3. J. J. Naughton, Geochemica et Cosmochimica Acta 37 1163 (1973).

4. T. Y. Chu, private communication to the author.

5. J. V. Beck, Transaction AIME, Paper 61-SA-27.

6. T. Gerlach, private communication to the author.

7. T. Gerlach, code A-078 reported in 1976 Cuba Symposium - Code lists, A. R. Iacoletti, SAND76-0246, Sandia Laboratories, Albuquerque, NM, October, 1976.

8. W. B. Murfin, "A Preliminary Model for Core/Concrete Interactions," SAND77-0370, in press, Nuclear Fuel Cycle Safety Research Department, Sandia Laboratories, Albuquerque, NM.

9. "Light Water Reactor Safety Research Program Quarterly Report, July-September 1976," SAND77-0214, Nuclear Fuel Cycle Safety Research Department, Sandia Laboratories, Albuquerque, NM, March 1977.

10. "Light Water Reactor Safety Research Program Quarterly Report, July-September 1975," SAND75-0632, Nuclear Fuel Cycle Safety Research Department, Sandia Laboratories, Albuquerque, NM, December 1975.

11. M. Peehs, "Investigations of Molten Corium Phases," International Atomic Energy Authority Report No. IAEA-SM-190/10, Kraftwerk Union Aktiengesellschaft, Erlangen, Germany, 1975, pp. 355-368.

12. "Reactor Safety Study-An Assessment of Accident Risks in U. S. Commercial Nuclear Power Plants," United States Nuclear Regulatory Commission Report No. WASH-1400 (NUREG-75/014), October 1975.

13. Roger O. Wooten, Battelle Columbus Laboratory, private communication, October 1976.

DISTRIBUTION:

USNRC Distribution System (306 copies)
NRC-3
Attn: Robert Wade
U.S. Nuclear Regulatory Commission
Washington, D. C. 20555

Dr. M. Fisher
Gesellschaft fur Kernforschung
Project Nuclear Safety (PNS)
75 Karlsruhe
Postfach 3640
Federal Republic of Germany

Dr. H. Holleck
Gesellschaft fur Kernforschung
PNS/IMF
75 Karlsruhe
Postfach 3640
Federal Republic of Germany

Dr. H. Albrecht
Gesellschaft fur Kernforschung
PNS/IRCH
75 Karlsruhe
Postfach 3640
Federal Republic of Germany

Dr. J. P. Hosemann
Gesellschaft fur Kernforschung
Project Nuclear Safety
75 Karlsruhe
Postfach 3640
Federal Republic of Germany

Professor of Mayinger
Lehrstuhl und Institut fur
Verfahrenstechnik
T.U. Hannover
3000 Hannover 1
Callinstr. 15 F
Federal Republic of Germany

M. F. Osborne
Gesellschaft fur Kernforschung
75 Karlsruhe
PNS/USNRC
Postfach 3640
Federal Republic of Germany

Gesellschaft fur Kernforschung (2)
PNS/RBT
75 Karlsruhe
Postfach 3640
Federal Republic of Germany
Attn: Dr. S. Hagen
D. Perinic

H. Seipel
BMFT
Federal Ministry for Research
and Technology
53 Bonn
Federal Republic of Germany

Dr. E. Herkommer
Institute for Reactor Safety
5000 Koln 1
Gloschengasse 2
Federal Republic of Germany

Professor Dr. H. Unger
IKE
University of Stuttgart
7 Stuttgart - Vaihingen
Pfaffenwaldring 31
Federal Republic of Germany

G. H. Kinchin
Safety & Reliability Directorate
Wigshaw Lane
Culcheth
NR Warnington, Chesire
England

Dr. M. Peehs
KWU
Abt. Rb. 3
852 Erlangen
Postfach 325
Federal Republic of Germany

Dr. M. Dalle Donne (2)
Kernforschungszentrum Karlsruhe
Institut fur Neutronenphysik
und Reaktortechnik
75 Karlsruhe 1
Postfach 3640
Federal Republic of Germany

Dr. H. Kottowski
c/o - Euratom Ispra
21020 Centro Euratom di Ispra
(Varese) Italy

Milad Matthias
Dept. of Nuclear Studies and Safety
Ontario Hydro
700 University Ave. (H-16)
Toronto, Ontario
Canada M5G1X6

764 312

Distribution (cont'd):

Division of Reactor Safety Research (8)
Office of Nuclear Regulatory Research
U.S. Nuclear Regulatory Commission
Mail Station: G158
Washington, DC 20555
Attn: M. Silberberg, Chief,
Experimental Fast Reactor Safety Branch
R. W. Wright, Experimental Fast
Reactor Safety Branch
R. DiSalvo, Fuel Behavior Branch (6)

U.S. Energy Research & Development Administration (4)
Reactor Safety Research Coordination
Washington, DC 20545
Attn: R. W. Barber, Actg. Director (3)
T. E. McSpadden, Project Manager

Operational Safety Division
U.S. Energy Research & Development Administration
Albuquerque Operations Office
P. O. Box 5400
Albuquerque, NM 87115
Attn: J. R. Roeder, Director

Argonne National Laboratory
9700 South Cass Avenue
Argonne, IL 60439
Attn: H. H. Hummel

Oak Ridge National Laboratory
Box Y, Bldg. 9201-3
Oak Ridge, TN 37830
Attn: M. H. Fontana

Brookhaven National Laboratory
Upton, LI, NY 11973
Attn: W. Y. Kato, Head,
Fast Reactor Safety Division

University of California (2)
Energy and Kinetics Department
5530 Boelter Hall
Los Angeles, CA 90024
Attn: W. E. Kastenberg
J. N. Castle

Department of Nuclear Engineering
University of New Mexico
Albuquerque, NM 87131
Attn: A. W. Cronenberg

University of Arizona (2)
Department of Nuclear Engineering
Tucson, AZ 85721
Attn: R. L. Seale
R. L. Brehm

1200 W. A. Gardner
Attn: K. J. Touryan, 1260
T. B. Lane, 1280
1262 H. C. Hardee
1262 D. W. Larson
1262 D. O. Lee
4010 C. Winter
5000 A. Narath
5160 W. Herrmann
5167 B. M. Butcher
5167 H. J. Sutherland
5167 J. E. Smaardyk
5262 K. L. Goin
5400 A. W. Snyder
5410 D. J. McCloskey
5411 D. A. Dahlgren (10)
5411 M. Berman
5411 R. K. Cole
5411 P. W. Conrad
5411 R. L. Knight
5412 J. W. Hickman
5412 L. D. Buxton (10)
5412 W. B. Murfin
5420 J. V. Walker
5422 R. L. Coats
5422 H. G. Plein
5423 J. E. Powell
5430 R. M. Jefferson
5443 B. D. Zak
5443 L. S. Nelson
5450 J. R. Reuscher
5451 T. R. Schmidt
5830 M. J. Davis
5831 N. J. Magnani
5831 D. A. Powers
5831 R. S. Sallach
5833 F. J. Zanner
5846 E. K. Beauchamp
9330 A. J. Clark, Jr.
9337 N. R. Keltner
8266 E. A. Aas (2)
3141 C. A. Pepmueller (Actg.) (5)
3151 W. L. Garner (3)
For ERDA/TIC (Unlimited Release)

764 315